

MULTISCALE AND MULTIPHYSICS MODELING OF PRESSURE DRIVEN
ISCHEMIA AND ULCER FORMATION IN THE SKIN

A Thesis

Submitted to the Faculty

of

Purdue University

by

Vivek Dharmangadan Sree

In Partial Fulfillment of the

Requirements for the Degree

of

Master of Science in Mechanical Engineering

May 2019

Purdue University

West Lafayette, Indiana

THE PURDUE UNIVERSITY GRADUATE SCHOOL
STATEMENT OF THESIS APPROVAL

Dr. Adrian Buganza Tepole, Chair

School of Mechanical Engineering

Dr. Thomas Seigmund

School of Mechanical Engineering

Dr. Elsje Pienaar

School of Biomedical Engineering

Approved by:

Dr. Jay P. Gore

Head of the School Graduate Program

TABLE OF CONTENTS

	Page
LIST OF FIGURES	v
ABSTRACT	vi
1 Introduction	1
1.1 Pressure Ulcers	1
1.1.1 Hypoxia in Skin from Mechanical Loading	1
1.1.2 Pressure Ulcer Formation From Hypoxia	3
2 Linking Microvascular Collapse to Tissue Hypoxia : A Multiscale Model of Pressure Ulcer Initiation	5
2.1 Anatomy and Microvasculature of Human Skin	5
2.2 Creation of Microvasculature Trees	6
2.3 Finite Element Model of the RVE	10
2.4 Oxygen Diffusion at the Tissue Scale	15
2.5 Results	19
2.5.1 Compression and Shear of the RVEs	19
2.5.2 Hypoxia at the Tissue Level	25
2.5.3 Effect of Skin Anatomy and Mechanical Properties on Pressure- Induced Hypoxia	27
3 Coupling an Inflammation Regulatory Network to a Tissue Scale Finite Element Model	31
3.1 Inflammation Network Model (0D)	31
3.1.1 Modeling Cell Populations	32
3.1.2 Modeling Inflammatory Variables	34
3.2 Tissue Scale Finite Element Model (3D)	36
3.3 Results	38
3.3.1 Keratinocyte-Neutrophil Subsystem	38

	Page
3.3.2 Pressure Ulcer Formation at the Tissue Scale	41
4 Conclusions, Discussion and Future Work	48
REFERENCES	56

LIST OF FIGURES

Figure	Page
2.1 Skin microvasculature geometry	7
2.2 Fractal generation algorithm	9
2.3 Generation of the RVE model	11
2.4 Five different RVEs resulting from performing the fractal generating algorithm and post-processing steps	14
2.5 RVE simulations	16
2.6 Tissue model with layers of skin	17
2.7 Compression and shear of a RVE	20
2.8 Extraction of the vasculature geometry as the RVE deforms	21
2.9 Change in volume fraction of the vasculature tree in response to compression and shear of the RVE	23
2.10 Tissue level simulations predict patterns of tissue hypoxia from applied pressure at the top surface of the skin	27
2.11 Parametric study showing the effect of changing the tissue stiffness μ and thickness t on the profiles of tissue hypoxia under applied pressure	30
3.1 a) Regulatory network implicated in pressure ulcer formation, b) Tissue scale axisymmetric model with coupled skin mechanics	32
3.2 Analysis of the circuit involving only the keratinocyte and neutrophil cell populations	37
3.3 Analysis of the network when the parameter $\lambda_{n,Da}$ is modified	40
3.4 Analysis of the circuit when the parameter $\lambda_{n,KC}$ is modified	41
3.5 Steady state contours of oxygen, cell species and cytokines as a function of applied pressure	42
3.6 Effect of changing the pressure magnitude and the radius of the compressed zone R_{disk}	45
3.7 Sensitivity of the average keratinocyte, ρ_k , and neutrophil, ρ_n , densities obtained from integration over the tissue scale domain	46

ABSTRACT

Dharmangadan Sree, Vivek M.S.M.E, Purdue University, May 2019. Multiscale and Multiphysics Modeling of Pressure Driven Ischemia and Ulcer Formation in the Skin. Major Professor: Adrian Buganza-Tepole.

Pressure ulcers (PU) are localized damage to skin and underlying tissue that forms in response to ischemia and subsequent hypoxia from external applied mechanical loads such as pressure, pressure in combinations with friction and shear. PUs are devastating injuries that disproportionately affect the older adult population. The initiating factor of pressure ulcers is local ischemia, or lack of perfusion at the microvascular level, following tissue compression against bony prominences. In turn, lack of blood flow leads to a drop in oxygen concentration, i.e, hypoxia, that ultimately leads to cell death, tissue necrosis, and disruption of tissue continuity. Despite our qualitative understanding of the initiating mechanisms of pressure ulcers, we are lacking quantitative knowledge of the relationship between applied pressure, skin mechanical properties as well as structure, and tissue hypoxia. This gap in our understanding is, at least in part, due to the limitations of current imaging technologies that cannot simultaneously image the microvascular architecture, while quantifying tissue deformation. We overcome this limitation in our work by combining realistic microvascular geometries with detailed mechanical constitutive models into a microscale finite element model of the skin. By solving boundary value problems on a representative volume element via the finite element method, we can predict blood volume fractions in response to physiological skin loading conditions (i.e., shear and compression). We then use blood volume fraction as a homogenized variable to couple tissue-level skin mechanics to an oxygen diffusion model. With our model we find that moderate levels of pressure applied to the outer skin surface lead to oxygen

concentration contours indicative of tissue hypoxia. In the second part of the thesis we explore the possibility of interlinking the model of tissue hypoxia with a cell regulatory network that governs the dynamics of PU formation. While there is a general understanding of the biological elements involved in this process and their interdependence within the biological PU signaling network, this system's spatio-temporal dynamics in conjugation with realistic geometries have not yet been studied. Here we first present a 0D mathematical description of the PU regulatory network consisting of two cell types - keratinocytes and neutrophils- and six chemical species - $\text{TNF}\alpha$, KC, ROS, DAMPs, O_2 and XO. Extension of this regulatory network from a set of ordinary differential equations to realistic spatial domains is demonstrated by coupling each species' dynamic equations to reaction diffusion partial differential equations. This model is further coupled to mechanical deformation of the spatial domain by including a pressure-sensitive oxygen perfusion term from the vascular deformations. The total model provides solutions to the regulatory network dynamics at the tissue scale with spatio-temporal detail on the evolution of each species. The model predicts patterns of PU formation in response to moderate loads, as seen clinically and experimentally. Future work will include rigorous calibration and validation of this model, which may render our work an important tool toward developing better prevention and treatment tools for pressure ulcers specifically targeted toward the older adult patient population.

1. INTRODUCTION

1.1 Pressure Ulcers

Pressure ulcers (PU) are localized tissue damage that leads to inflammation and necrosis of skin and underlying tissue due to lack of oxygen resulting from blood flow reduction in response to applied external mechanical loading. Pressure ulcers also referred to as bed sores or decubitus ulcers as the names suggest forms when skin tissue is subjected to prolonged periods of applied external pressure loads or pressure in combination with friction or shear. Pressure ulcers are a serious medical condition, affecting more than 3 million individuals annually in the US, and leading to health care costs of approximately 16 billion dollars every year [1]. Pressure ulcers occur predominantly among the older adult population. In fact, between 7.3% and 23% of adults in nursing homes in Europe and the United States are affected by pressure ulcers [2]. It is now indisputable that a primary mechanism of pressure ulcer initiation is ischemia, or lack of blood perfusion. Ischemia leads to low oxygen concentration in the tissue, denoted hypoxia, triggering a cascade of inflammatory signals that culminate in ulceration. [3–6]. However, despite this knowledge, prevention of pressure ulcers remains extremely challenging [7]. One reason for the difficulty in assessing pressure ulcer risk for an individual is that a quantitative connection between applied pressure, skin mechanical properties and anatomy, and tissue hypoxia has remained elusive.

1.1.1 Hypoxia in Skin from Mechanical Loading

Technologies such as laser Doppler flowmetry enable clinicians to monitor skin perfusion and detect hypoxic levels that could lead to ulceration. However, these tools

are expensive and out of reach for the general population [8]. Moreover, they provide an average measurement of oxygen concentration across the entire tissue thickness and offer no detail about the underlying mechanisms of pressure-driven ischemia [9–11]. From investigation of the skin microvasculature we have gained detailed knowledge of the vascular tree irrigating the skin [12–14]. Yet, *in vivo* imaging and characterization of microvasculature collapse as tissue deforms remains out of reach. Our knowledge of skin mechanical properties has also improved significantly in recent years, both through traditional *ex vivo* tests [15], and novel noninvasive *in vivo* tests [16, 17]. Unfortunately, knowledge of an individual’s skin mechanical behavior alone is also insufficient to anticipate the levels of perfusion inside the skin in response to applied pressure.

High fidelity computational models of soft tissue deformation and perfusion with realistic geometries and material properties can fill the gap in the current available imaging technologies. Computational models of skin mechanics have already permeated into the field of reconstructive surgery because of the importance of stress on wound healing [18–20]. Skin, like most connective soft tissues, shows remarkable mechanical behavior [21]. It behaves as a nearly incompressible solid in time scales on the order of seconds, but shows stress relaxation and compressibility in the time scales going from minutes to hours [22–24]. The mechanical behavior of skin in the short time scales has been modeled extensively within a hyperelastic framework [25, 26]. Multiphasic formulations accounting for interstitial fluid have been employed, although to a lesser extent, to model the stress relaxation in the longer timescales [27]. Computational modeling of blood flow in the microvasculature has received some attention [28], but these efforts have not accounted for the mechanical behavior of the skin and the link to the deformation and collapse of the vasculature. In fact, few computational studies have been carried out in the context of pressure ulcer formation accounting for the vasculature [29, 30]. While these efforts have been an important step towards a better understanding of pressure-driven ischemia, they have been limited to simplified, two-dimensional geometries. Additionally, these investiga-

tions focused on the mechanical response of skin and not on the link to hypoxia, which is the indisputable initiator of pressure ulcers. Therefore, there is a lack of models that explicitly consider the microstructure of the skin including the microvasculature, and how mechanical deformation can alter blood perfusion leading to hypoxia.

Another important aspect in the study of pressure ulcer formation is identifying the underlying biology of cell signalling that governs the dynamics of pressure ulcer formations. Hence our study also attempts to bridge the hypoxia to the dynamics of pressure ulcer formation by exploring the regulatory network and its dynamics from a systems biology perspective. Furthermore such a study would be incomplete without bridging these two discrete studies and combine them to understand the formation of PUs across different length and time scales which is presented in Chapter 3.

1.1.2 Pressure Ulcer Formation From Hypoxia

In response to hypoxia, native skin cells called Keratinocytes release a chemotactic signals, primarily Keratinocyte Chemokine (KC) and monocyte chemoattractant protein 1 (MCP-1), which attract inflammatory cells such as neutrophils and macrophages [31]. Subsequently, neutrophils infiltrate the tissue and release tumor necrosis factor alpha ($\text{TNF}\alpha$), which leads to keratinocyte death. Keratinocyte necrosis, in turn, releases damage associated molecular patterns (DAMPs) which further recruit neutrophils, initiating a perpetual cycle of inflammation that eventually leads ulcer formation [32]. The neutrophil population can also contribute to a sudden increase in reactive oxygen species (ROS) in what is referred to as an oxidative burst [33]. Moreover, during ischemia xanthine dehydrogenase (XDH) is converted into xanthine oxidase (XO) [34], which produces the ROS superoxide anion and hydrogen peroxide [35]. ROS further contribute to cell necrosis.

To better understand PU formation and progression, mathematical models have been developed. For example, agent based models are popular and convenient as their implementation is straight-forward [36]. However, it is difficult to analyze the

signaling network topology from these models. On the other hand, mathematical models based on ordinary differential equations (ODEs) provide an alternative to studying the dynamics of a cell regulatory network [37]. An advantage of the ODE approach is the ability to study the network motifs and their implication for the overall dynamics of the system. Furthermore, ODE descriptions may be a stepping stones towards developing more complex and realistic models that can capture spatio-temporal dynamics, as shown in a PU formation model.

In chapter 3 we present a cell signalling network and associated ODE mode of pressure ulcer formation and demonstrate how such a simplified model can encompass all essential dynamics of pressure ulcer formation. Further in the chapter we also address the present knowledge gap of how the cell signalling network can be incorporated into a tissue scale finite element analysis of hypoxia in skin from Chapter 1 by developing more general PDE descriptions of the cell regulatory interactions that are readily suited for such coupled multifield numerical analysis. The PDE model describes reaction diffusion equations governing the kinetics and spatial distribution of all cell and chemokines along with Oxygen which is coupled to a applied mechanical loading and tissue vascular collapse.

Finally we close the thesis with a conclusion and discussion chapter outlining important results from Chapters 2 and 3 on how the model captures the dynamics of complex bio-mechanical problem. While this work sheds light into the governing mechanisms involved in the formation of PUs it is now means complete and comprehensive as more work needs to be done in order to thoroughly validate the results presented here with experiments. In this regards the future works for this study includes calibrating and validating the model parameters discussed in Chapters 2 and 3 with *in-vivo* experiments on murine and human skin.

2. LINKING MICROVASCULAR COLLAPSE TO TISSUE HYPOXIA : A MULTISCALE MODEL OF PRESSURE ULCER INITIATION

2.1 Anatomy and Microvasculature of Human Skin

Human skin is organized in multiple layers with different mechanical and biological properties [38,39]. The outer-most layer of the skin is called epidermis and is primarily comprised of keratinocyte cells. The epidermis in itself is subdivided into two general sub layers. The first sublayer of epidermis is called stratum corneum, and is formed by dead keratinocytes [40]. The second sublayer is denoted viable epidermis, providing a niche for the living epidermal cells. The stratum corneum is formed as keratinocytes terminally differentiate within the viable epidermis and move up to the outer surface [41]. The epidermis is avascular and a considerable portion of oxygen supply to the outer layers is in the form of diffusive uptake from the surrounding air [42]. More oxygen and nutrients for the epidermis are obtained through diffusion from the middle layer of the skin, the dermis, which is the layer of skin immediately below the epidermis [41]. The dermis is structurally constituted by stiff collagen fibers and acts as the primary load bearing member of human skin [26,43]. It is also much thicker than the epidermis . The dermis can be further sub-classified into three sublayers; the papillary dermis attached to the epidermis, a sub papillary, intermediate layer, and the reticular layer, connecting the skin to the underlying fat and muscle [44].

Microvasculature in the human skin mostly resides in the dermis and forms two distinct horizontal plexus. The lower plexus is formed by perforating vessels from subcutaneous tissue that enter the reticular dermis. This layer is connected to an upper plexus through arterioles and venules ascending and descending, respectively, to and from the skin surface. These vessels undergo multiple subdivisions along their up-

ward path, forming the upper horizontal plexus which also contains the capillary loops connecting the venules and arterioles inside the papillary dermis [12, 13]. Braverman et al. have characterized the anatomy of these vessels by spatially reconstructing optical microscope images $1\mu\text{m}$ thick sections of skin biopsies. Figure 2.1a shows the structure of blood vessels in the skin as reported in their work [12, 13]. These and other studies have shown that the vasculature structure in the skin is fractal in nature [14, 45]. Indeed, fractals are a recurring pattern in some biological structures, such as vascular networks in most tissues including the skin [46, 47], the Purkinje networks in the human heart [48], and the airways in the lungs [49]. Cevc et al [14] for instance, have measured the change in vessel number, diameter, and length as the vascular tree undergoes multiple bifurcations along the skin thickness. In this paper, we generate fractal trees with the same characteristics as the skin’s microvasculature (Figure 2.1b), and use these geometries in a microscale model of the skin in order to increase our understanding of pressure-induced ischemia through microvascular collapse.

2.2 Creation of Microvasculature Trees

We use a space-filling fractal generation algorithm to create realistic vasculature trees. Our algorithm follows from previous work on fractal generating algorithms in two dimensions that were designed to generate the Purkinje fiber networks of the human heart [50]. Other, similar work, includes two-dimensional fractals of blood vessel geometries [28], and space filling fractal tree generation in three dimensions to model the airways [49].

To create the fractal network of the microvasculature, we first choose a progenitor node and a random growth direction. We then initiate a branch creation loop. The flowchart of the algorithm is shown in Figure 2.2a. Once the first branch attains a required length and reaches the *End branch growth* condition in Figure 2.2a, we stop growing this branch, bifurcate the tree and start the growth of two new branches

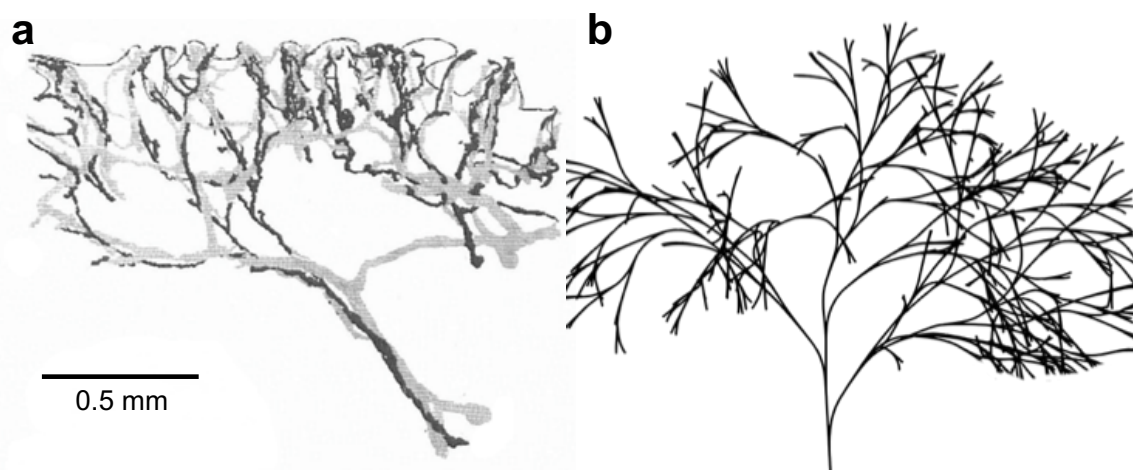


Fig. 2.1. Skin microvasculature geometry. a) Reconstructed image of the skin microvasculature from slices of skin biopsy using an optical microscope adapted from [13]. The skin is made out of two horizontal plexus that form a fractal tree structure. b) Our fractal generating algorithm leads to realistic microvasculature geometries.

from the terminal node of the original branch. This loop continues for a required number of generations which is decided apriori. While initially there is one branch to grow, this number increases exponentially with more generations of the tree. All the branches that need to grow at a particular instant during the execution of the algorithm are stored in a *To-Grow* list. There are several instances in the algorithm in which randomness is incorporated. One of those instances is the order in which branches are grown. The *To-Grow* list is shuffled every time a branch reaches the *End branch growth* condition in Figure 2.2a, before the growth of the next branch.

Following initialization of a branch, the algorithm enters a loop that grows the branch in the direction \vec{r} at each new iteration $i+1$. The vector \vec{r} is chosen so that the tree is space filling and random [50, 51]. To achieve these features, \vec{r} is computed at each iteration by summing three contributions with different weights: i) the branch tends to continue growing in the previous direction \vec{r}_i ; ii) the branches are biased to grow in the direction \vec{d}_g , the unit vector aligned with the closest distance vector between the current branch and all other branches, iii) there is a random contribution \vec{r}_{rand} (Figure 2.2b).

The termination of the branch growth algorithm in Figure 2.2a also includes a random input. As the branch grows, we compute the branch length value l_b , which measures the arc length of a branch. The final branch length needed in Figure 2.2a to determine whether or not to end the growth of the current branch is assumed to be a random variable, normally distributed, with a mean branch length $l_{b,avg}$ and a standard deviation σ_{lb} . The parameters $l_{b,avg}$ and σ_{lb} may be independent for each branch. To match the skin microvasculature, for example, we decrease the mean branch length $l_{b,avg}$ for successive generations of the tree. Branch growth can be terminated even if the branch has not achieved the required length, if the distance between the current branch and any other branch in the tree is less than a predetermined tolerance ($\varepsilon = 1\mu\text{m}$). In this case the growth of a branch is terminated due to collision with another branch, and no new branches emerge from this terminal node.

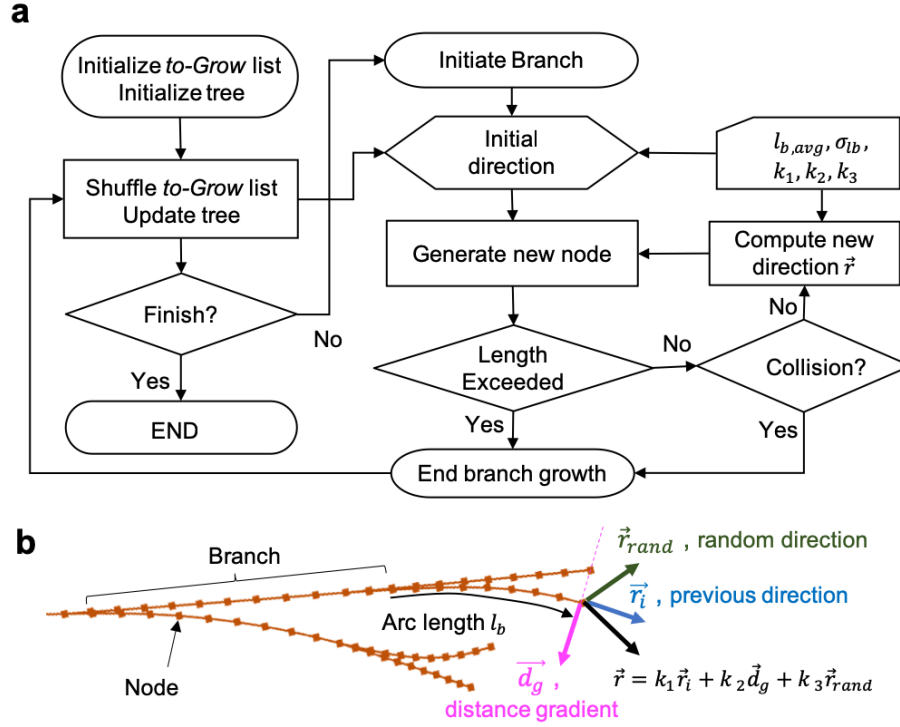


Fig. 2.2. Fractal generation algorithm. a) Flowchart defining the growth of the tree and also the subroutine for a single branch. Once a branch is initialized, it grows by a node at each iteration. The branch growth terminates if the branch collides with another branch or if the branch arc length exceeds a threshold length drawn from a normal distribution of lengths controlled by parameters $l_{b,avg}, \sigma_{lb}$. b) At each iteration, the branch grows in the direction \vec{r} determined from the sum of three contributions: i) previous growth direction \vec{r}_i , ii) negative of the closest distance vector to any other branch in the tree \vec{d}_g , iii) random contribution \vec{r}_{rand} . The parameters k_1, k_2, k_3 control the new direction \vec{r} .

The parameters of the algorithm can be modified to make sure that the fractals replicate the properties of the skin vasculature. Skin is characterized by blood vessels with lengths on the order of $100\mu\text{m}$ for the initial, lower levels of the tree. From these initial vessels, there are 8 to 10 bifurcations along the thickness direction, each leading to a decrease in length of around 40 percent, such that the top plexus is composed of vessels with lengths of about $10\mu\text{m}$. In this model we do not resolve the vessels into the level of single capillaries since we expect that collapse of the larger $10 - 20\mu\text{m}$ diameter vessels will be a major factor in ischemia, although further refinements into even smaller scales can be achieved at the expense of greater computational resources. Our modeling assumption is supported by observations in microangiograms of small vessels in nailfolds subjected to compressive strain [52]. In these experiments, blood flow was cut off even at the top plexus, i.e. before reaching the capillary loops connecting venules and arterioles.

The final volume fraction of vasculature is on the order of $\phi_0 \sim 0.5\%$ [53–55]. Additionally, vessel diameters reported in [14] indicate that the vessels in the middle and upper generations of the tree are in the range $10 - 30\mu\text{m}$.

In summary, the fractal growth algorithm is controlled by 5 parameters. The length of the different branches is governed by the parameters $l_{b,avg}$ and σ_{lb} . Following the discussion of the previous paragraph, we set $l_{b,avg} = 100\mu\text{m}$ for the originating branch, and reduce this value by 40 percent at each bifurcation. We set $\sigma_{lb} = 0.01l_{b,avg}$ and keep it constant during the entire execution of the algorithm. The remaining 3 parameters controlling the algorithm are k_1 , k_2 , and k_3 , which appear in the expression for \vec{r} (see Figure 2.2b). The value of the parameters used here are $k_1 = 1$, $k_2 = 0.1$, $k_3 = 0.05$.

2.3 Finite Element Model of the RVE

From a fractal tree generated with the algorithm described in the previous section, we generate a RVE of the skin in several steps as shown in Figure 2.3. Figure 2.3a

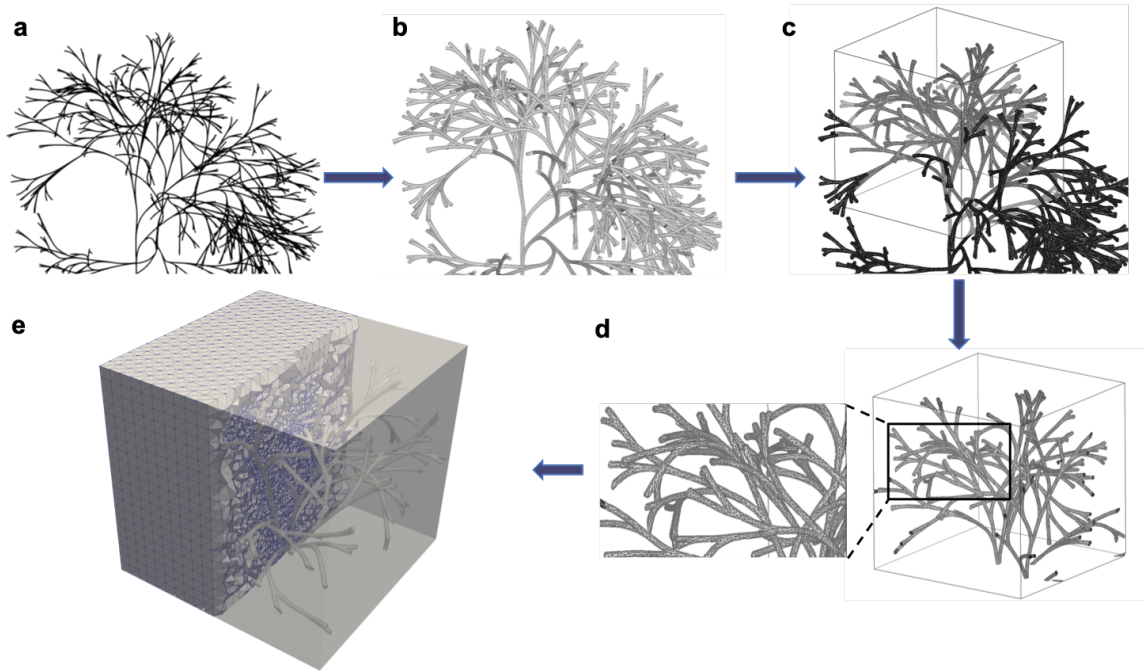


Fig. 2.3. Generation of the RVE model. a) A tree of the microvasculature generated with our fractal algorithm. b) Solid cylinders are generated for each branch of the tree, and then combined into a single solid. c) We fit a smooth, closed surface to the solid tree using the Poisson reconstruction algorithm, and embed the surface into a solid 1mm^3 cube. d) We subtract the tree from the cube to generate the RVE. e) The geometry is meshed with tetrahedra. For the tree shown, the mesh consists of 203,697 nodes and 1,208,437 elements.

shows a typical fractal tree representing the skin vasculature. First, we convert this tree to a three-dimensional CAD model as shown in 2.3b using the software FreeCAD [56]. More specifically, since the fractal tree defines the center line of the blood vessels, we execute a script in FreeCAD to sweep cylinders along each branch. The diameter of these cylinders is set to $20\mu\text{m}$. A Boolean union operation combines each of these cylinders into a single solid structure. Then, in an additional step, we fit a closed and smooth surface to the union of all cylinders using the Poisson surface reconstruction algorithm. We are not interested in the vasculature itself, but instead on the tissue surrounding the vasculature. Thus, we embed the surface reconstruction of the vessel tree into a solid 1mm^3 cube and perform a Boolean subtraction operation (Figure 2.3c). The final result from these processing steps is shown in Figure 2.3d. The inset showcases the detail of the vessel structures. The CAD model is exported as an IGES file, and imported into the commercial finite element software package Abaqus Standard for meshing and analysis. A typical mesh used in our simulations is shown in Figure 2.3e. The mesh shown consists of 203,697 nodes and 1,208,437 tetrahedral elements.

Due to the inherent randomness incorporated into the fractal generation algorithm, we can generate different vascular geometries even from the same initial conditions and parameter set. Five such geometries are shown in Figure 2.4. The volume fraction of the vascular trees is indicated alongside each geometry in Figure 2.4. The range of volume fractions across the different RVEs is well in agreement with the typically observed blood volume fraction in human skin [14, 53].

We discretize the RVE geometries using linear tetrahedral (C3D4) elements in Abaqus. Contact constraints are introduced along the inner walls of the microvasculature using the elastic, surface to surface contact feature in Abaqus. These contacts are necessary to prevent unrealistic deformations such as interpenetration due to the displacement and deformation of the vessel walls.

Skin is commonly modeled as a hyperelastic material, and a number of strain energy functions have been proposed to model skin's mechanical response [24, 57].

There are material models that consider the presence of a collagen fiber network in the material of interest, some of which have been applied to skin [58–60]. In this study, however, we opt for an isotropic Neo-Hookean description, similar to previous studies [61], for two reasons. First, while skin does exhibit anisotropy, the dispersion of the fiber network in this tissue is relatively large [62]. Moreover, under compression, the type of loading relevant for pressure ulcer formation, it is reasonable to expect little contribution from the collagen fibers, which can only resist tensile loading and buckle under compression [63]. Thus, we use the strain energy density function of the form

$$\Psi = C_{10}(\bar{I}_1 - 3) + \frac{1}{D_1}(J - 1)^2, \quad (2.1)$$

where $C_{10} = \mu_0/2$, μ_0 is the shear modulus, \bar{I}_1 is the first invariant of the isochoric part of the right Cauchy-Green deformation tensor, $J = \det(\mathbf{F})$ is the volume change, with \mathbf{F} the deformation gradient, and $D_1 = 1/K$, where K is the bulk modulus. From previous experimental studies on skin [64] the estimated baseline parameters for the Neo-Hookean model are $\mu_0 = 75$ KPa and $K = 350$ kPa.

Normal compression and shear deformation of the human skin are the most important deformation modes implicated in pressure ulcer formation [65]. Therefore, we perform simulations directly controlling compressive and shear strains on the RVE. To obtain the response of skin under these types of deformation, we enforce periodic boundary conditions on all outer surfaces except for the top and bottom surfaces. For the compression simulation, the displacement is specified at the top surface of the RVE while the bottom surface is constrained in the z direction, resulting in the compressive stretch λ_z (Figure 2.5a). For the shear simulation, the bottom is again held fixed while Dirichlet boundary conditions are applied to the top surface in lateral direction, leading to a shear strain γ_{xz} (Figure 2.5b).

The primary variable of interest obtained from the simulations is the deformed volume fraction occupied by the deforming blood vessels, ϕ . This volume fraction is related to the total blood volume within the skin. Thus, we are interested in how

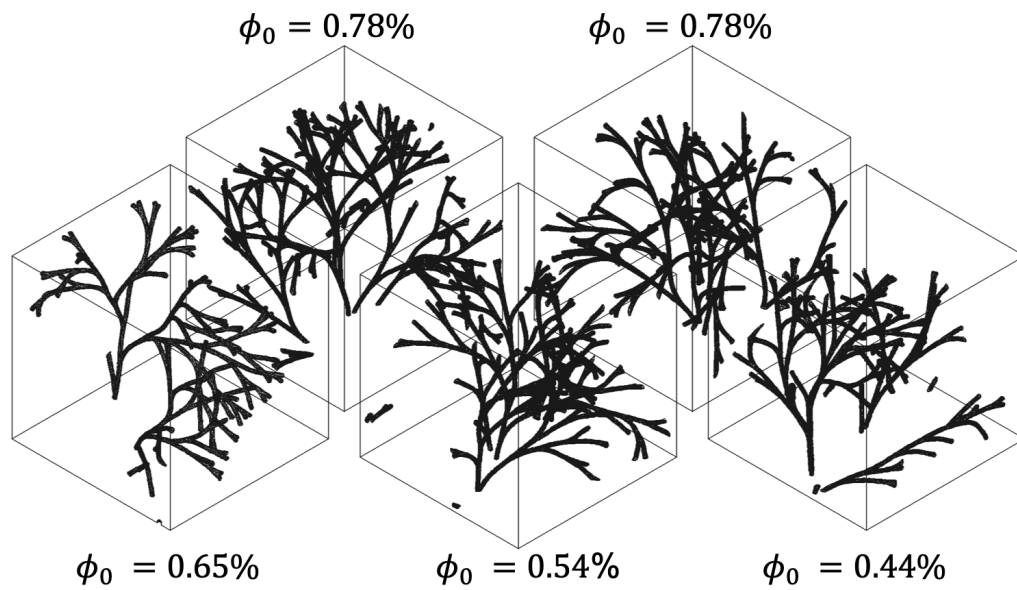


Fig. 2.4. Five different RVEs resulting from performing the same fractal generating algorithm and post-processing steps. The variation in the trees is due to the incorporation of random inputs in the fractal algorithm. The volume fraction for the RVEs, ϕ_0 , is within the physiological values for skin.

this variable changes as the RVE deforms. Since the initial blood volume fraction, ϕ_0 , is different for each of the RVEs in Figure 2.4, we compute the normalized change in volume fraction: $\hat{\phi} = \phi/\phi_0$. This normalization also enables us to calculate an average response as a function of deformation, regardless of the specific value of ϕ_0 . Thus from a set of simulations for different values of λ_z and γ_{xz} , we seek functions $f_1 : \lambda_z \rightarrow \hat{\phi}$ and $f_2 : \gamma \rightarrow \hat{\phi}$ that describe the average response of the normalized volume fraction of blood under compression and shear.

2.4 Oxygen Diffusion at the Tissue Scale

One of the key goals of the proposed simulation framework is to link the deformation of the skin to tissue hypoxia through the prediction of microvascular collapse. We thus introduce a tissue-level model of skin ischemia mechanics. For the tissue level simulations we use Comsol Multiphysics, a commercial finite element solver. Figure 2.6 shows an axisymmetric domain of skin tissue. We model three different layers according to the skin anatomy. The top layer is the stratum corneum, with a thickness of 0.02mm. The second layer is the viable epidermis, with a thickness of 0.1mm. The bottom layer is the dermis tissue, and in this case the initial thickness is $t_0 = 1.38\text{mm}$ [57, 66, 67]. The domain considered has a radius of $r_o = 25\text{mm}$. The domain is discretized using quadratic quadrilateral serendipity elements.

In the tissue level model, we solve for the oxygen concentration distribution with a homogenized diffusion equation. We also solve the linear momentum balance equation to obtain the tissue deformation as the tissue is subjected to relevant loading conditions. The mechanical behavior of the tissue is described with the Neo-Hookean strain energy introduced in Equation 2.1. Since the domain considered is axisymmetric, the fixed boundary conditions are $u_r = 0$ at $r = 0\text{mm}$, and $u_z = 0$ at $z = -1.5\text{mm}$. The top of the domain has a compressive pressure applied along $r \in [0, 5]\text{mm}$. In the oxygen diffusion partial differential equation, the primary variable is the transcutaneous oxygen partial pressure P_{O_2} , which indirectly measures the oxygen concentration in

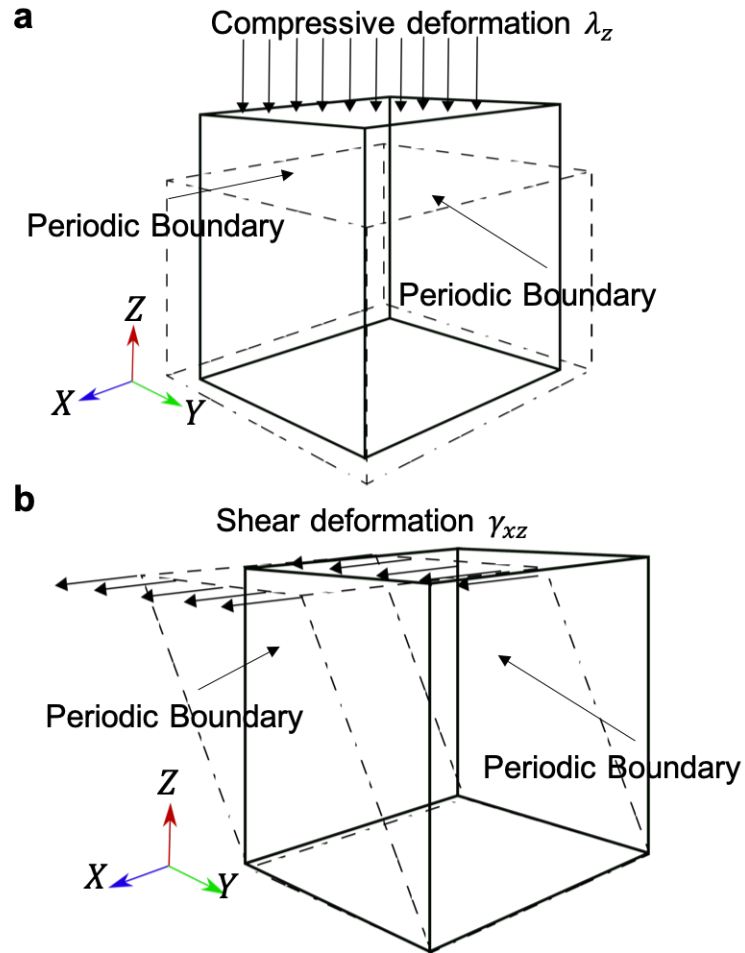


Fig. 2.5. RVE simulations. a) We apply a normal compressive strain λ_z by controlling the relative displacement between the top and bottom surfaces of the RVE, the lateral surfaces satisfy periodic boundary conditions. b) Shear is applied to the RVE by controlling the x -displacement of the top surface with respect to the bottom surface, while maintaining periodic boundary conditions on the lateral surfaces of the RVE.

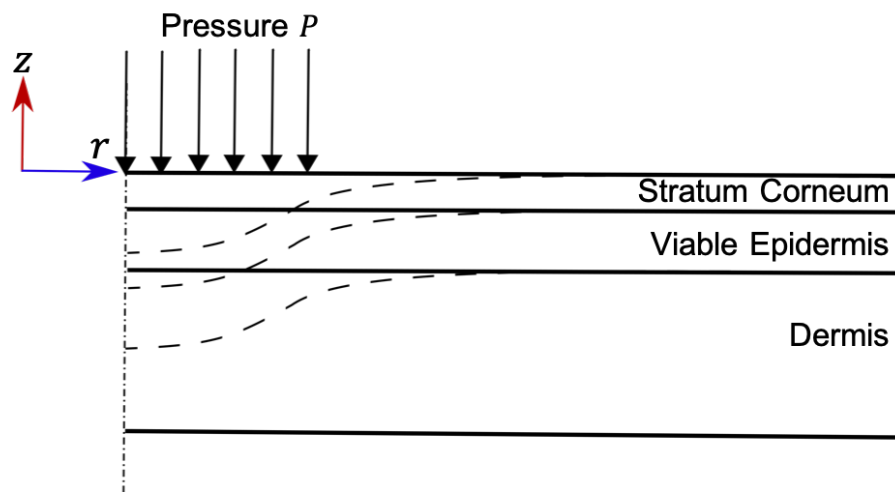


Fig. 2.6. Tissue model with layers of skin. We consider an axisymmetric domain with outer radius of 5cm. Three skin layers are considered: stratum corneum, viable epidermis, and dermis. The bottom of the domain is constrained, whereas a normal pressure load is applied at the center of the domain $r \in [0, 5]$ mm

the skin. Partial oxygen pressure is also the most common directly observed quantity reported in previous experimental studies related to skin hypoxia [9–11]. The reaction diffusion equation solved for the oxygen partial pressure is

$$\alpha \frac{dP_{O_2}}{dt} + \nabla \cdot \mathbf{q} = s_{P_{O_2}}, \quad (2.2)$$

where dP_{O_2}/dt is the material time derivative, $\mathbf{q} = D\alpha\nabla P_{O_2}$ is the flux assumed to follow Fickian diffusion with diffusivity $D\alpha$, and $s_{P_{O_2}}$ is the source term. Note that no advective transport of oxygen is explicitly considered. The diffusivity of oxygen is given by the diffusion coefficient D and the oxygen solubility α . Here, $D = 1.5 \times 10^{-3} \text{mm}^2/\text{s}$, and $\alpha = 3 \times 10^{-5} \text{mm}^3\text{O}_2/\text{mm}^3\text{mmHg}$ in the germinal layer of epidermis and in the dermal tissue [68]. For the stratum corneum, these parameters are assumed to be an order of magnitude less to account for low water content in the cells: $D = 1.5 \times 10^{-4} \text{mm}^2/\text{s}$ and $\alpha = 3 \times 10^{-6} \text{mm}^3\text{O}_2/\text{mm}^3\text{mmHg}$ [68, 69]. The physiological oxygen source rate is assumed to be $s_0 = 0.8 \times 10^{-5} \text{s}^{-1}$ and no production or consumption term is assumed in the stratum corneum due to the absence of living cells. The baseline oxygen source term is assumed such that the contours match physiological reported conditions.

The key coupling term between deformation and ischemia is the source term $s_{P_{O_2}}$. We assume that the source term is proportional to the normalized volume fraction of blood vessels in the tissue. This now enables us to link the deformation simulations of the RVEs to the tissue scale hypoxia model. At any point in the domain we can retrieve the amount of normal compression λ_z and shear γ , and evaluate the homogenized functions $f_1 \equiv \hat{\phi}_1$ and $f_2 \equiv \hat{\phi}_2$ as defined in the previous section. The modified source term is then computed based on our prediction of the deformed volume fraction: $s_{P_{O_2}} = \hat{\phi} s_0$.

2.5 Results

2.5.1 Compression and Shear of the RVEs

We first subject the RVEs shown in Figure 2.4 to compressive strains and focus on the deformation of the microvasculature. Figure 2.7a shows the contours of the normal component of the strain tensor, E_{zz} , over the outer boundary of the domain. The columns from left to right show the sequential compression of the tissue as the top surface of the RVE is displaced to produce the average stretch λ_z . Although only a single RVE is shown, the behavior is similar in all five RVEs. The overall strain contours on the boundary of the domain are fairly homogeneous. The second row in Figure 2.7a shows multiple cross sections of the domain. In the cross sections it is apparent that even though the E_{zz} contours are constant over large portions of the domain, there are localized strain concentrations close to the vessels, which is indicative of the large deformations that the vessels undergo compared to the surrounding material.

Isolating the deformed vessel geometry reveals that some vessels collapse at moderately low RVE stretch λ_z . This is further illustrated in detail in Figure 2.8a-b. The reference configuration of one of the RVEs is shown in Figure 2.8a together with the corresponding detail of the vessel surface. Figure 2.8b then shows the same RVE after a compression of $\lambda_z = 0.8$. We highlight that with these levels of overall stretch some of the vessels collapse, as seen the inset in Figure 2.8b.

The application of the normal stretch is accompanied by in plane deformation, allowable based on the periodic boundary conditions. In combination, the deformation of the lateral surfaces of the RVE and the normal stretch λ_z lead to a change in the volume occupied by the RVE. By extracting the deformed vessel geometry (Figure 2.8b), we compute the volume change associated to the microvasculature alone. For the RVE shown in Figure 2.7a the initial volume of the vasculature is 0.00782mm^3 , and the final volume is 0.00373mm^3 . A more detailed analysis of the change in normalized volume fraction is presented later in this section.

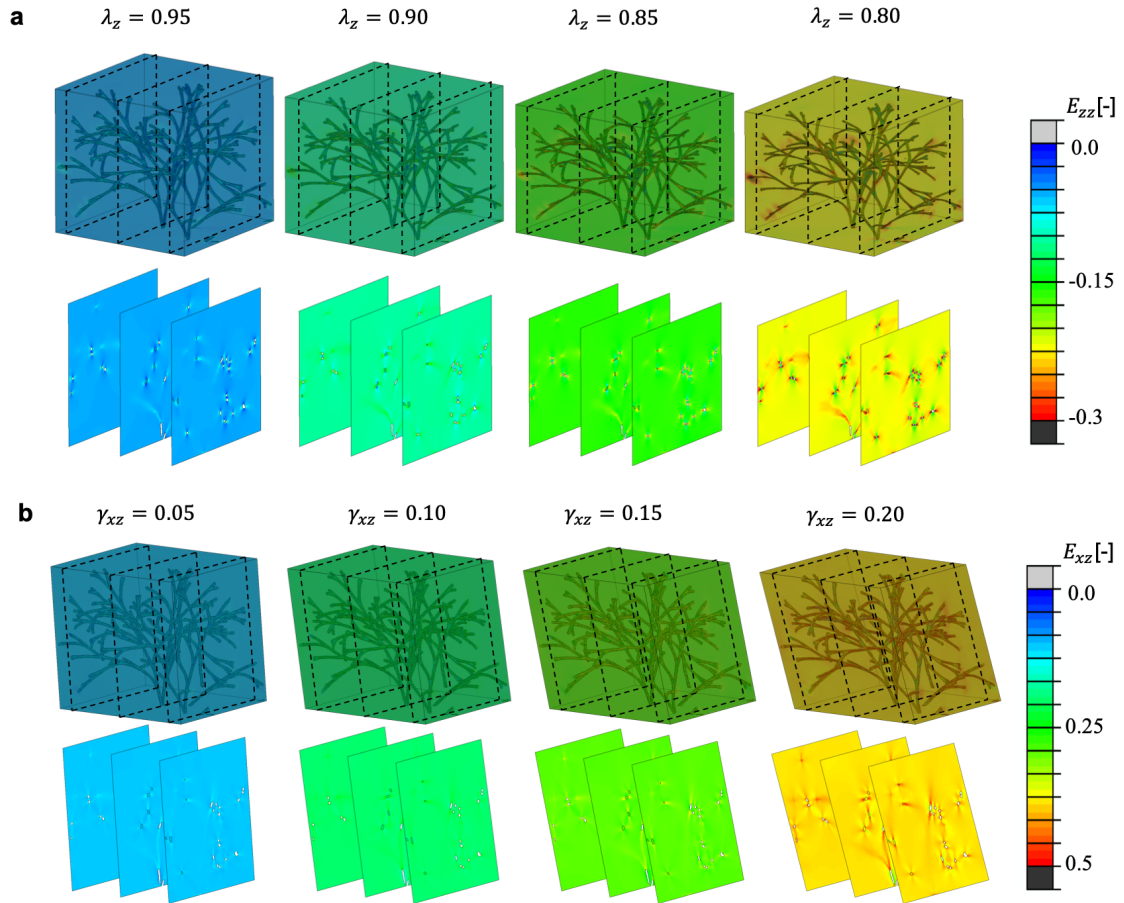


Fig. 2.7. Compression and shear of a RVE. a) Sequence of snapshots of the RVE compression simulation. The contours of the normal component of the Green Lagrange strain, E_{zz} are homogeneous over most of the domain, but cross sections reveal higher strains surrounding the blood vessels. b) Snapshots of an RVE subjected to increasing shear γ_{xz} . Once again, the E_{xz} of the Green Lagrange strain tensor appears constant over the domain, with cross sections showing that there are high strains surrounding the vascular tree.

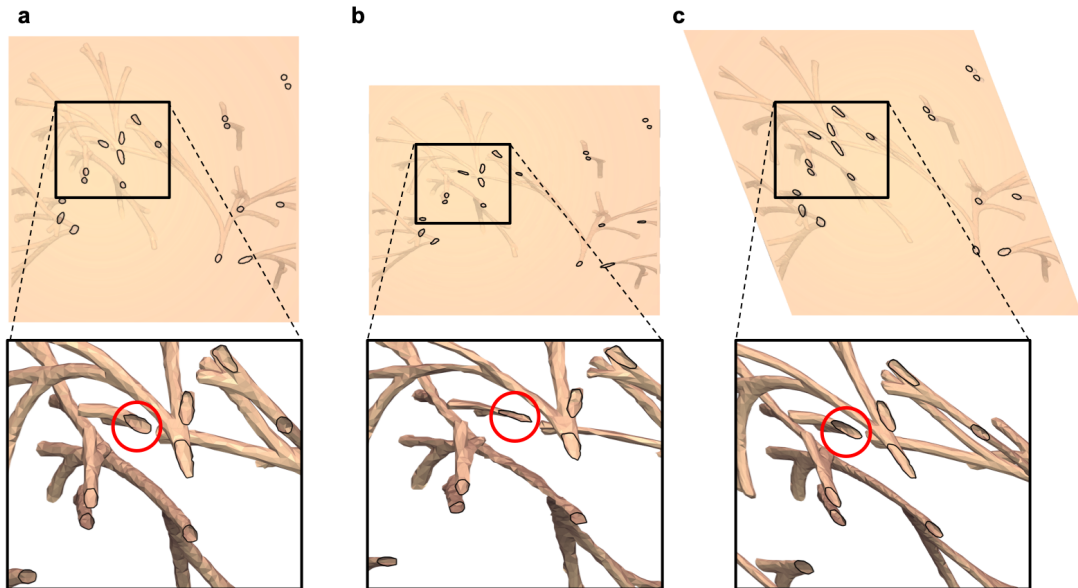


Fig. 2.8. Extraction of the vasculature geometry as the RVE deforms. a) The reference configuration of one of the RVEs and the corresponding detail of the vasculature tree. b) The result of one compression simulation up to λ_z . Isolating the deformed vessel geometry we compute the change in volume fraction as well as identify the collapse of some of the vessels. c) Deformed tree due to RVE shear γ_{xz} . The inset shows that even at high shear the vessels deform but do not fully collapse.

The result from a shear deformation simulation for one of our RVEs is depicted in Figure 2.7b. Analogous to the compression simulation, applying an average shear γ_{xz} to the entire RVE by prescribing the displacement of the top and bottom surfaces and periodic boundary conditions on the lateral surfaces, results in overall homogeneous strain contours as seen in the sequence of snapshots of Figure 2.7b. Similar to the compression case, upon closer inspection it becomes apparent that there are localized regions of higher shear strain, E_{xz} , near the vessels (Figure 2.7b). However, in contrast to the compression case, when the RVE is subjected to simple shear, the vessels do not undergo complete closure even under large values of γ_{xz} . Isolating the vessel geometry and magnifying the detail of the deformed tree illustrates the shape changes that are typically seen for the vessels. The cross section of the vasculature becomes elongated but the vessels do not collapse (Figure 2.8c).

We focus on the vasculature volume fraction as the homogenized variable of interest because this variable is linked to the total blood volume in the skin tissue. It is also reasonable to assume that the amount of blood contained within the distributed vascular network at any time is proportional to the source term for the oxygen diffusion model, as explained in the Methods section. Then, a reduction in volume fraction of the vascular tree indicates that the total blood volume in the tissue decreases and causes a corresponding decrease in the oxygen availability. The volume fraction of the blood vessels is calculated on the deformed vasculature surfaces isolated from the deformed RVEs as shown in Figure 2.8.

Figure 2.9a shows the change in volume fraction of blood vessels due to applied compressive stretch λ_z . Since each RVE geometry in Figure 2.4 has a different volume fraction in the reference configuration due to the randomness incorporated into the fractal generation algorithm, the change in volume fraction is not directly comparable across RVEs. To obtain a single function $f := \hat{\phi}_1(\lambda_z)$ describing the average RVE response, we normalize the volume fraction values by the initial volume fraction of each RVE. The results for the normalized volume fraction are shown in Figure 2.9b. Interestingly, this normalization collapses the volume fraction change of all the RVEs

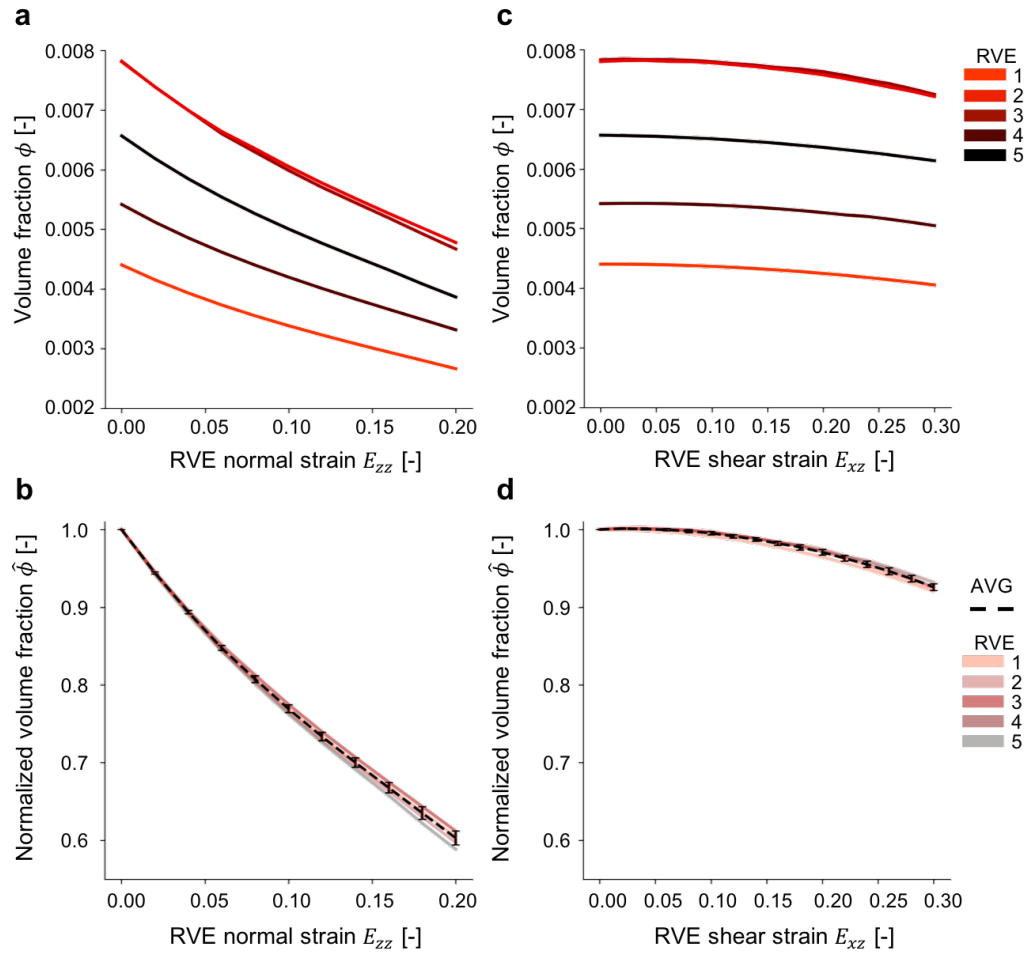


Fig. 2.9. Change in volume fraction of the vasculature tree in response to compression and shear of the RVE. a) Absolute change in the volume fraction of the vascular tree when the RVE is subjected to compression. Different curves indicate RVEs with different volume fraction due to the randomness incorporated in the tree generation. b) Normalized volume fraction curves collapse into a single response for all 5 RVEs considered, revealing that a 20% compressive strain leads to more than 40% reduction in normalized blood volume fraction. c) Shear causes a small change in volume fraction of the different RVEs. d) Normalized volume fraction curves for the RVE shear simulations also collapse into a single response with very little deviation between the different RVEs.

into a single response, with very little deviation among the different curves. From Figure 2.9b it is easier to observe the degree to which the normal stretch causes reduction in blood volume. Application of 20% compressive strain leads to a drop of about 40% of the normalized volume fraction. If we consider the fact that some blood vessels may have completely collapsed at intermediate points in the tree, occluding any blood flow to the vessels further along in the tree, as reported before [52], the actual blood volume may be even less than our initial estimate. Thus, our estimate of the blood volume fraction could be seen as a conservative indicator of blood perfusion.

As noted before, the applied shear strain on the RVE causes deformation of the vessels, but rarely does it lead to collapse. Therefore, the change in volume fraction for the shear simulations is smaller compared to the compression cases. Figure 2.9c shows the change in volume fraction with increasing shear for the five different RVEs. Similar to before, we compute the corresponding normalized change in volume fraction. Upon normalization, the curves collapse into a single response depicted in Figure 2.9d, just as it was the case for the compression simulations. We note that the shear induced normalized volume fraction change is only about 10% for shear strains of 30%. This indicates that compression may be a more relevant mode of deformation to cause ischemia compared to simple shear.

We use the average of the curves plotted in Figure 2.9b and Figure 2.9d to approximate the function linking vessel volume change to the oxygen source term in the diffusion model. For the compression deformation we have the polynomial fit

$$\hat{\phi}_1 = -14.061\epsilon_z^3 + 7.5901\epsilon_z^2 - 2.926\epsilon_z + 0.992, \quad (2.3)$$

while for the shear deformation we have

$$\hat{\phi}_2 = -0.055\gamma_{xz}^3 - 0.9492\gamma_{xz}^2 + 0.0419\gamma_{xz} + 1.0003. \quad (2.4)$$

Due to the substantially smaller contribution of shear to blood volume change, and considering situations at the tissue scale in which skin is mostly under a large

compressive strain but small shear, we ignore the contribution from $\hat{\phi}_2$ in the tissue simulations and consider only the function $\hat{\phi}_1$ to link both scales.

2.5.2 Hypoxia at the Tissue Level

We first ensure that the tissue scale model of oxygen diffusion matches the physiological steady state profiles of oxygen concentration. To set this baseline condition, we use the tissue scale model described in the Methods section but we do not apply any loading at the top surface. Setting the oxygen source term to $s_{P_{O_2}} = s_0 = 0.8 \times 10^{-5} \text{s}^{-1}$ in the dermis, we obtain the oxygen concentration profile shown in Figure 2.10a, top. This contour matches the expected *in vivo* profiles reported experimentally and from other numerical modeling efforts [42, 68, 69]. The outer layer of the skin is in contact with the atmosphere and is thus exposed to an oxygen partial pressure of $P_{O_2} = 160 \text{mmHg}$. The region on the top surface of the epidermis where the pressure load is applied is not in contact with the atmosphere and the boundary condition for this part of the top boundary is $P_{O_2} = 0 \text{mmHg}$.

The oxygen contours in the top panel of Figure 2.10a show that, in the physiological setting, the viable epidermis receives some oxygen from the atmosphere, but there is a sharp gradient and the oxygen partial pressure drops to about $P_{O_2} = 40 \text{mmHg}$ at the interface between the viable epidermis and the dermis. The dermis also shows a gradient of oxygen concentration in the physiological state. However, since the dermis domain has the source term representing the oxygen supplied by the blood, the gradient is only significant at the top of the dermis, a continuation of the gradient from the epidermis, but the concentration quickly settles to a value of $P_{O_2} = 60 \text{mmHg}$ in most of the dermis domain.

When pressure is applied at the top, the tissue deforms substantially, see Figure 2.10a. To couple this deformation to the oxygen source term we use the function $s_{P_{O_2}} = \hat{\phi}_1(\lambda_z)s_0$. Note that the $\hat{\phi}_1$ function is defined at every location of the domain, and hence will introduce a spatial heterogeneity in the model even though the

underlying response $\hat{\phi}_1$ comes from the set of simulations with the multiple RVEs under a range of normal strains. Figure 2.10a shows the representative contours of the oxygen concentration when the compressive pressure at the top surface is 25 and 50 kPa. Increasing the pressure leads to greater hypoxia, as expected. For the 25kPa case we see that the central region, right under the part of the boundary where pressure is applied, shows a reduction in partial oxygen pressure of about 30 percent. The gradient is not constant through the thickness but rather it shows an hourglass shape. Nevertheless, the hypoxic region is mostly confined to the column of tissue under compression. This hourglass shape can be expected from diffusion of oxygen from the surrounding tissue into the compressed tissue. At 50kPa the oxygen in the central region is further diminished. In conclusion, applied normal pressure leads to a significant reduction of oxygen concentration, despite of the surrounding tissue being well perfused.

The plot in Figure 2.10b illustrates the variation of the oxygen partial pressure along the thickness direction $z \in [0, -1.5]$ mm at the the centerline of the domain $r = 0$ mm. The point at the epidermal surface at the top of the domain, where the pressure boundary condition is applied, is not in contact with the atmosphere and hence $P_{O_2} = 0$ mmHg at this point. Oxygen concentration increases through the epidermis and in the interface between stratun corneum and viable epidermis, $z = -0.02$ mm, partial pressure of oxygen is 40mmHg in the absence of loading, but it drops to 15mmHg as pressure is applied. The most extreme changes in the oxygen profile occur in the dermis. In the middle of the dermis, at $z = -0.75$ mm for instance, the oxygen partial pressure goes from 65mmHg to 18mmHg as the pressure load is increased to 50kPa.

The plot in Figure 2.10c shows the integral of the oxygen profile along the centerline as a function of applied pressure at the top surface. Namely, Figure 2.10c results from integrating the curves in Figure 2.10b. The relationship is nonlinear, with a very steep decrease initially compared to at higher pressures. This averaging over the

entire thickness better illustrates the significance of our results: the oxygen partial pressure drops from 60mmHg to 20mmHg as the applied pressure increases to 50kPa.

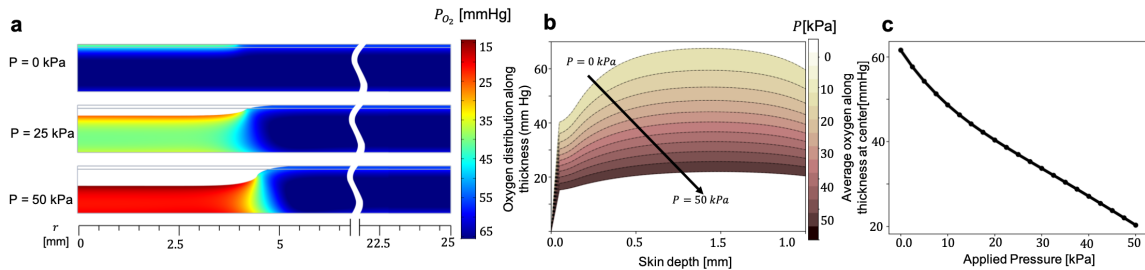


Fig. 2.10. Tissue level simulations predict patterns of tissue hypoxia from applied pressure at the top surface of the skin. a) Contours of partial oxygen pressure P_{O_2} for different loading conditions. When no load is applied the oxygen profile shows a sharp gradient across the stratum corneum and the epidermis, but the partial oxygen pressure achieves a near constant value for the dermis due to the presence of a source term in this domain. As pressure is applied, the tissue is compressed. We link the normal strain to the oxygen source term through our homogenized vessel volume fraction variable from the RVE model. As a result, we predict patterns of tissue hypoxia. b) Plots of oxygen concentration at the centerline of the domain for different pressures. The drop in partial oxygen pressure is most significant in the dermis. c) Integrating the curves in b) summarizes the effect of applied pressure on oxygen concentration. As pressure increases up to 50kPa, our model predicts a drop of more than 60% in oxygen partial pressure.

2.5.3 Effect of Skin Anatomy and Mechanical Properties on Pressure-Induced Hypoxia

Pressure ulcers are more common in the older adult population. However, the exact way in which aging increases the susceptibility to pressure ulcers is not fully understood. There are indications that biological changes in inflammation with age affect pressure ulcer progression [70]. There are also behavioral factors involved in the increased susceptibility to pressure ulcers with aging [71]. Here we are interested

in factors that may play a role in the susceptibility to ischemia, the initiation step of pressure ulcers. In particular, changes in skin anatomy and mechanical properties with age have been reported [72,73], but whether or not these changes could affect susceptibility to ischemia remains unsolved. We therefore decided to use our multiscale model to increase our understanding of how changes in skin anatomy and mechanical properties can influence the pressure-induced hypoxia profiles. Our parameter study focuses on the shear modulus μ and the thickness t . The value of the shear modulus used up to this point, $\mu_0 = 75\text{kPa}$, is representative of adult skin [64]. The thickness value used thus far, $t_0 = 1.5\text{mm}$, is also representative of adult skin [57]. We apply a pressure of 30kPa at the top surface of the skin, analogous to previous simulations, but we change the thickness over the range $t/t_0 \in [0.5, 2]$, and the shear modulus over the range $\mu/\mu_0 \in [0.5, 2]$.

Figure 2.11 summarizes the results of our parametric study. Changes in the mechanical properties of skin have a marked influence on the oxygen concentration profiles. Qualitatively, the contours look similar to those in Figure 2.10a. Hypoxia is mostly confined to the column of tissue right below the portion of the top boundary where pressure is applied. The hypoxic region continues to show the hourglass shape encountered in Figure 2.10a. As the shear modulus increases, however, it can be noticed that the hypoxic regions are not evenly distributed but occur mostly at the upper and lower ends of the dermis. Even though the oxygen profiles are of similar shape to those seen in Figure 2.10a, the values change significantly with a change in shear modulus compared to the baseline. As could be expected, weaker skin, i.e. $\mu < \mu_0$, leads to higher strains and therefore more severe tissue hypoxia. Stiffer skin leads, as intuited, to less hypoxic conditions. The plot in Figure 2.11b shows the integral of the oxygen concentration over the centerline of the domain. Interestingly, this curve is nonlinear, showing that variation from our initial estimate μ_0 towards a stiffer value only has a moderate effect on the oxygen partial pressure, whereas decreasing μ_0 from the nominal value yields a more drastic change in oxygen partial pressure.

From the parametric study concerning t , we see that an increase in thickness is beneficial, i.e. it protects the tissue against hypoxia. The opposite also holds, thinning of the dermis leads to a decrease in the oxygen contours with applied pressure. The contours continue to be qualitative similar compared to those in Figure 2.10a. Yet, as the thickness increases, the hypoxic regions are not constant through the entire thickness, but are rather concentrated at the top and bottom of the dermis. Figure 2.11d then shows the integral of the oxygen profile along the centerline. Here it can be seen that reducing the thickness with respect to the nominal value has a marked effect on the oxygen concentration, whereas increasing the thickness shows a moderate increase in the partial oxygen pressure at the center of the domain. Regardless, it should also be noted that while the sensitivity of the oxygen curves are similar for both parametric studies, it is the variation in the shear modulus that produces the most significant changes in the oxygen contours.

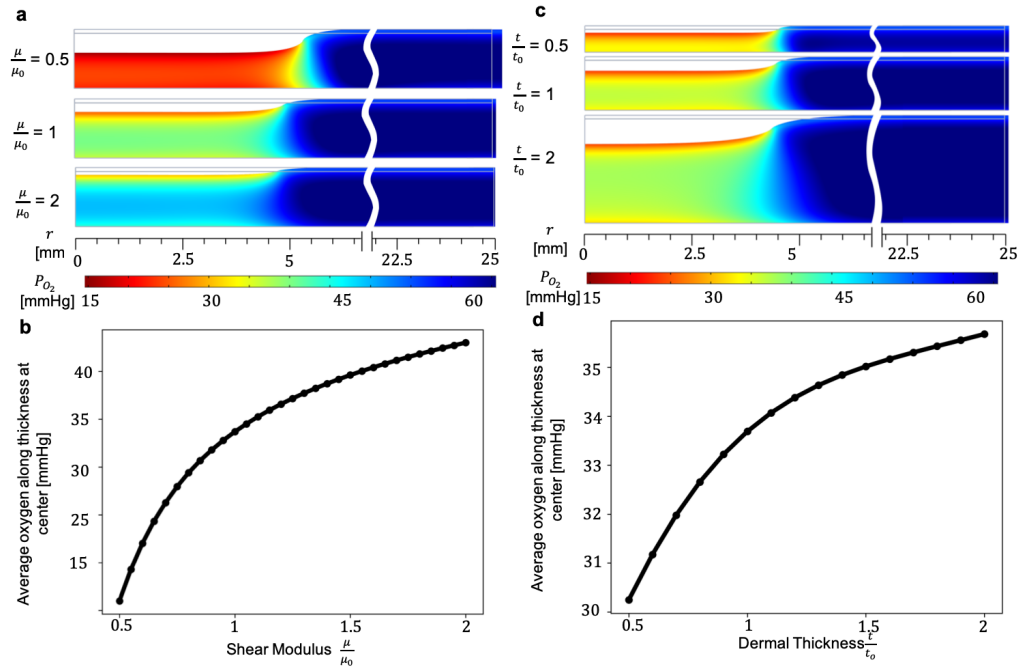


Fig. 2.11. Parametric study showing the effect of changing the tissue stiffness μ and thickness t on the profiles of tissue hypoxia under applied pressure. a) A weaker skin, $\mu < \mu_0$ shows a higher degree of hypoxia but a similar contour to those observed with the baseline parameters. A stiffer skin, $\mu > \mu_0$ has the opposite effect on the contour values. b) Averaging the oxygen concentration at the center and plotting the result against the normalized changes in the shear modulus we see that the tissue model of oxygen diffusion is very sensitive to a decrease in μ . c) Changing the dermis thickness leads also to a change in hypoxia values under applied load. As thickness increases, hypoxic regions become more pronounced at the top and bottom of the dermis. Increasing thickness leads to less severe hypoxia compared to a decrease in thickness. d) Integrating the oxygen profile at the center as thickness changes reveals that the amount of hypoxia is less sensitive to a variation in thickness compared to the sensitivity of the oxygen profiles to tissue's shear modulus.

3. COUPLING AN INFLAMMATION REGULATORY NETWORK TO A TISSUE SCALE FINITE ELEMENT MODEL

The starting point of our model is a simplified description of the signaling network implicated in PU formation. Following similar approaches as introduced in computational systems biology [37, 74–76], we consider a system of ODEs to describe the 0D pressure ulcer dynamics. This enables us to investigate the basic operating principles of the biological system, i.e., how the topology of the network leads to its specific functions and features. To inform the ODEs we identify ranges of parameter from literature reports and study the network’s sensitivity to changes in these parameters. We then expand our analysis beyond ODEs to realistic domains by introducing PDEs that describe the interaction of the cells and chemical species within the signaling network with their spatial environment. This last step in our description of PU formation is crucial to coupling the underlying biological control to deformation of the tissue domain and to coupling the regulatory network to a pressure-sensitive oxygen source term, i.e., to vascular collapse.

3.1 Inflammation Network Model (0D)

The system consists of cell populations and chemical concentrations (Fig.3.1a). Specifically, we include the cell species keratinocytes (ρ_k) and neutrophils (ρ_n). Additionally, we include the chemical species oxygen (Ox), KC and MCP-1 (Kc), DAMPs (Da), $TNF\alpha$ (Ta), ROS (Ro), and XO (Xo). Cell numbers or chemokine concentrations are generally reported as non-dimensional values or as fold-changes. Therefore, to compare our model to published experimental work, all variables are considered non-dimensional in this study. For keratinocytes, $\rho_k = 1$ is the healthy state while for

the inflammatory cells $\rho_n = 1$ is the upper bound during ulceration. For physiological partial oxygen pressures $Ox = 1$. Contrarily, the inflammatory species Ta , $Ro = 1$ correspond to a state of chronic ulceration. For Xo we assume that the total concentration of XO and XDH is constant such that Xo is normalized with respect to this value and thus falls within the range $[0, 1]$. A typical fraction of XO in the healthy state is $Xo = 0.15$ [35]. The variable Da is normalized such that $Da = 1$ would be achieved at maximum necrosis rate with $\rho_k = 1$.

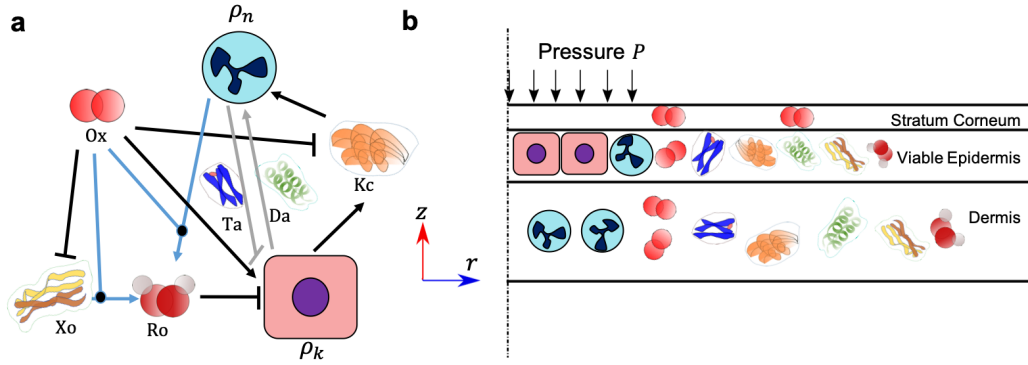


Fig. 3.1. a) Regulatory network implicated in pressure ulcer formation. Keratinocytes (ρ_k) respond to low oxygen (Ox) by releasing keratinocyte chemokine (Kc), which recruits neutrophils (ρ_n). Neutrophils produce $TNF\alpha$ (Ta), which impairs keratinocyte proliferation and results in production of DAMPS (Da). Chemical signals XO (Xo) and ROS (Ro) also contribute to keratinocyte necrosis. b) Tissue scale axisymmetric model with coupled skin mechanics, oxygen transport, and reaction-diffusion equations capturing the regulatory network. Three skin layers are considered. Pressure is applied at the top of the domain.

3.1.1 Modeling Cell Populations

The keratinocyte population evolves in time according to [36, 37, 74, 77]

$$\dot{\rho}_k = p_k \cdot Hi(Ox) \cdot \rho_k \cdot \left(1 - \frac{\rho_k}{\rho_{k,max}}\right) - d_k \cdot (1 + \lambda_{k,Ta} Hi(Ta) + \lambda_{k,Ro} Hi(Ro)) \cdot \rho_k . \quad (3.1)$$

The parameter p_k is the production rate, which may be interpreted as the rate of cell division. For a single cell it has been reported to be $p_k = 0.028[1/\text{hr}]$, which we adopt here [78]. The function $Hi(X)$ is a sharp Hill function capturing the decrease in proliferation following hypoxia,

$$Hi(X) = \frac{X^n}{X_h^n + X^n}, \quad (3.2)$$

with X_h being the concentration at which $Hi(X_h) = 0.5$, and n being a parameter that dictates how fast the function changes from zero to one. Based on [79], keratinocytes proliferation is not impaired until oxygen levels drop below 40% of physiological partial oxygen pressure. Thus we set $Ox_h = 0.2$, and $n = 4$ to get $Hi(Ox) = 1$ for $Ox = 1$, then $Hi(Ox)$ stays close to this value as oxygen decreases, but as $Ox < 0.4$, the function $Hi(Ox)$ starts decreasing rapidly. We chose the basal apoptosis rate as $d_k = 0.014$ to ensure that the steady state, i.e., the physiological state, maintains a healthy keratinocyte population, i.e., $\rho_k = 1$. Moreover, based on literature reports, we set $\rho_{k,max} = 2$ [77]. The effective decay rate of keratinocytes is increased by the inflammatory signals Ta and Ro through a sum of Hill functions [37]. The parameters associated with increased necrosis of keratinocytes in response to inflammation are the concentrations X_h and the multipliers λ , which are the main degrees of freedom in this model. The multipliers are constrained to remain within the range $[0, 1]$. For $Hi(Ta)$, $\lambda_{k,Ta}$ is bound to be in the range $[0.1, 0.35]$ [80–82]. Similarly, for $Hi(Ro)$ $\lambda_{k,Ro}$ is bound to be in $[0.1, 0.4]$ [83, 84]. In all cases we set $X_h = 0.5$ and $n = 3$ enforcing that moderate levels of the inflammatory chemokines, below 20% of the values observed in pressure ulcers, will not induce significant damage. However, as inflammatory chemokines higher concentrations, the Hill function parameters ensure an increased effect on the keratinocyte population viability.

The neutrophil population is described with

$$\dot{\rho}_n = p_n \cdot (1 + \lambda_{n,Da}Hi(Da) + \lambda_{n,KC}Hi(Kc)) \cdot \rho_n \cdot \left(1 - \frac{\rho_n}{\rho_{n,max}}\right) - d_n \cdot \rho_n \quad (3.3)$$

Neutrophils respond to damage proteins Da [85] and the chemotactic signal Kc . We assume that the activation of neutrophils approaches its maximum value for non-dimensional values of $Da = 1$ and $Kc = 1$. We further assume that the neutrophil population saturates at $\rho_{n,max} = 2$ [74]. The neutrophil apoptosis rate is fast, on the order of $d_n = 0.14[1/hr]$ [86]. Chronic wounds show more than 40-fold increase in neutrophil numbers requiring a maximum activation $\lambda_{n,Da}Hi(Da) + \lambda_{n,KC}Hi(Kc) \geq 1$. The production rate is calculated to be $p_n = 0.141 [1/hr]$ to satisfy $\rho_n = 0.025$ in healthy skin. For the DAMPs activation we set $X_h = 0.3$ for $Hi(Da)$, and $X_h = 0.5$ for $Hi(Kc)$ and the exponent to $n = 3$ in both cases. The relative influence between damage and ischemia in the recruitment of neutrophils is critical. As a starting point we choose $\lambda = 0.5$ for both functions, but will analyse the sensitivity of the system dynamics to these parameters in detail.

3.1.2 Modeling Inflammatory Variables

Oxygen is supplied to the dermis by the dermal microvasculature from where it diffuses to the epidermis and is locally taken up by the keratinocytes. In the 0D model only, we model the rate of change of oxygen in the epidermis as

$$\dot{Ox} = -c_{Ox,k} \cdot Ox \cdot \rho_k + D_{Ox}(Ox_d - Ox) \quad (3.4)$$

where the consumption rate is $c_{Ox,k} = 22.93[1/hr]$ [42], $D_{Ox} = 22.68 [1/hr]$ serves as a diffusion parameter [42, 87], and Ox_d is the oxygen level in the dermis.

TNF α is produced by neutrophils [88] according to

$$\dot{Ta} = p_c \cdot \rho_n - d_c \cdot Ta \quad (3.5)$$

The decay of this and other chemokines is set to $d_c = 0.144[1/hr]$ [74]. When the neutrophils are at the maximum, $\rho_n = 1$, the inflammatory signal peaks at $Ta = 1$, thus requiring $p_c = 0.144[1/hr]$. In the steady state $Ta = \rho_n$.

Neutrophils and macrophages are recruited to the ulcer site in response to hypoxia as skin resident cells release MCP-1 and KC [31]. Here we consider the action of both chemokines in the single variable Kc which evolves in time according to

$$\dot{Kc} = p_c \cdot Hi(1 - Ox) \cdot \rho_k - d_c \cdot Kc \quad (3.6)$$

where the function $Hi(1 - Ox)$ is close to zero for $Ox = 1$ and increases as oxygen decreases. We set $X_h = 0.4$ for this function such that at $Ox = 0.6$ the rate of Kc release is half of the maximum. Hence, before keratinocytes necrosis increases (which is set to start at $Ox = 0.4$), keratinocytes will release the inflammatory signal. In addition to KC, neutrophils also infiltrate the wounded tissue following release of DAMPs by the necrotic keratinocytes. While DAMPs represent various molecules, we lump them into one variable in our model. We describe Da by

$$\dot{Da} = p_a \cdot (\lambda_{k,Ta} Hi(Ta) + \lambda_{k,Ro} Hi(Ro)) \cdot \rho_k - d_c \cdot Da \quad (3.7)$$

where the production follows from keratinocyte death due to inflammation and the effect of ROS, but ignores regular apoptosis [89]. The production rate is set to $p_a = 0.23$ [1/hr] such that at the peak inflammatory signal, if the cell population stayed constant at $\rho_k = 1$, Da would also reach one.

ROS are produced by two main sources, XO and neutrophils [90]. XO can serve as substrate for the production of ROS at a maximum rate of 40 nmol/min for peak XO and oxygen concentration [35]. Neutrophils produce 30nmol/min [35] at peak neutrophil and oxygen concentrations $\rho_n = 1$, $Ox = 1$. We model these processes as

$$\dot{Ro} = p_{R,X} \cdot Hi(Xo) \cdot Ox + Hi(Ox) \cdot p_{R,n} \cdot \rho_n - d_R Ro \quad (3.8)$$

where it should be noted that ROS production requires oxygen. For instance, neutrophils produce ROS only if the oxygen concentration is at least 30% of physiological values [91] and will increase with oxygen concentration. This is captured with the Hill function $Hi(Ox)$ where we set the parameters $X_h = 0.6$ and $n = 4$. The Hill function for Xo reaches a maximum when $Xo = 1$. Based on [33], chronic wounds

lead to ROS concentrations between 10 to 100 μ M. Thus, by normalizing with an intermediate value 50 μ M we set the production rate to $p_{R,n} = 0.036$ [1/hr] and a maximum value of $Hi(Xo)$ of 0.048 [1/hr]. Moreover, we estimate the decay rate as $d_R = 0.084$ [1/hr].

The total concentration of XO and XDH is assumed fixed and their sum equaling one [92]. Thus, we model Xo as

$$\dot{Xo} = (1/\tau) \cdot (1 - Hi(Ox)) \cdot (1 - Xo) - d_X Xo. \quad (3.9)$$

In the absence of ischemia, a commonly chosen value is $Xo = 0.15$ [92], while the time constant τ is on the order of a few hours, e.g., 2 to 6 [35]. According to [93] a value of $Ro < 0.2$ is necessary for physiological cell function. We therefor enforce $Xo = 0.15$ under physiological conditions by setting $X_h = 0.25$ in $Hi(Xo)$ in Eq. (3.8).

3.2 Tissue Scale Finite Element Model (3D)

In order to extend the 0D model dynamics captured by ODEs to realistic domains we can modify our model to incorporate spatial derivative terms to include reaction-diffusion leading to a set of PDEs. To further couple our model to the tissue scale mechanics of skin, we tie the oxygen source term to the local tissue compressive strain, thus, effectively incorporating vascular collapse under external loading. As a consequence, this modification will render external loading, tissue compression, and, subsequently, oxygen concentration the key drivers of pressure ulcer initiation.

Fig.3.1b shows an axisymmetric model of skin detailing its layers including their resident cell- and chemical species. Specifically, we model the stratum corneum as having a thickness of 0.02 mm, the viable epidermis as having a thickness of 0.1mm, and the dermis as having a thickness of 1.38mm. In sum, all layers give our skin model a total thickness of 1.5mm [57, 66, 94]. The entire domain is assumed to have a radius of $r_0 = 25$ mm.

The key coupling term between the regulatory network and the mechanics of skin at the tissue scale is the source term in the oxygen diffusion model. In particular, deformation is linked to the partial oxygen pressure through the source term $s_{P_{O_2}}$. Compressive strain in the tissue is believed to drive microvascular collapse inducing ischemia and hypoxia [95]. Based on our current work on multiscale models of pressure ulcer initiation, we assume the following relationship for the oxygen source term: $s_{P_{O_2}} = \hat{\phi} s_o$, with $s_o = 0.8 \times 10^{-5} \text{s}^{-1}$ and $\hat{\phi}$ a function obtained from simulations of microvascular collapse,

$$\hat{\phi} = -14.061\epsilon_z^3 + 7.5901\epsilon_z^2 - 2.926\epsilon_z + 0.992 . \quad (3.10)$$

Therefore, as applied pressure compresses the tissue, the normal strain component ϵ_z drives the reduction in the oxygen source term.

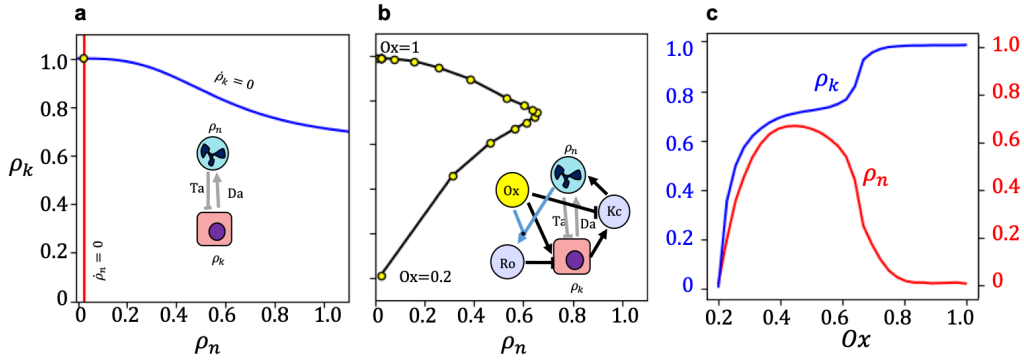


Fig. 3.2. Analysis of the circuit involving only the keratinocyte and neutrophil cell populations. a) The simplest possible subsystem considering only the direct interaction between keratinocytes and neutrophils. The two nullclines, $\dot{\rho}_n = 0$ in red, and $\dot{\rho}_k = 0$ in blue, are plotted in the phase space. There is a single steady state at (0.025, 1). b) The stable point moves in the phase portrait for an extended subsystem as a function of oxygen concentration. The extended subsystem accounts also for ROS and KC. c) The steady state of neutrophil and keratinocyte densities as a function of oxygen.

Similar to oxygen, each of the cell and chemical species obeys a reaction-diffusion equation of the form

$$\frac{dC_i}{dt} + \nabla \cdot \mathbf{q}_i = f_i, \quad (3.11)$$

where C_i is the concentration of each of the species in the tissue. The source term f_i follows directly from the ODE equations describing the system dynamics introduced before. The flux term $\mathbf{q}_i = D_i \nabla C_i$ is of Fickian diffusion nature and describes the transport of the species in the tissue. Since we are interested in the formation of pressure ulcers and not the subsequent wound healing or re-epithelialization, we don't consider migration of keratinocytes within the epidermis; hence, $D_{\rho_k} = 0$. Neutrophils diffuse towards the hypoxic keratinocytes in response release of KC and Da with a diffusivity of $D_{\rho_n} = 1 \times 10^{-9} \text{cm}^2/\text{s}$ [96, 97]. Due to the absence of active transport systems, we assume that the diffusivity of chemokines is much smaller than that of oxygen. Therefore, we use $D_i = 1 \times 10^{-6} \text{cm}^2/\text{s}$ for the chemical signals [96, 98].

3.3 Results

We start by analyzing the system of ODEs representing the regulatory network. This allows us to carefully investigate the role of the different parameters and the expected behavior of the 0D behavior before looking at the response of the system in a 3D spatial domain.

3.3.1 Keratinocyte-Neutrophil Subsystem

The motif involving the neutrophils and keratinocytes depicted in Fig. 3.1a is a composite negative feedback loop that stabilizes the signal and produces a robust steady state. Fig. 3.2a, shows the nullclines of the subsystem, $\dot{\rho}_k = 0$, $\dot{\rho}_n = 0$, in the phase-space of keratinocytes and neutrophils. The intersection of the nullclines represents the steady state at $\rho_k = 1.0$ and $\rho_n = 0.025$. It should be noted that the neutrophil nullcline is almost a straight line, such that the system favors low inflammation at high oxygen. We incrementally add to the complexity of the analysis by incorporating changes in oxygen concentration. The inset in the middle panel shows

the extended network including oxygen, KC and ROS. We compute the steady state at different oxygen values. In other words, we fix the oxygen concentration to a desired value and determine the steady state by finding the intersection of the nullclines in the neutrophil-keratinocyte phase space as a function of oxygen concentration. Fig. 3.2b thus shows how the steady state moves in the phase space as oxygen decreases. Alternatively, Fig. 3.2c depicts the steady state of keratinocytes and neutrophils as a function of oxygen. Keratinocyte population density decreases, first slowly and then very rapidly, as oxygen starts to approach $Ox = 0.2$. At $Ox = 0.2$, as discussed in the choice of parameters for the keratinocyte population, the proliferation rate is close to zero and the keratinocyte population vanishes. The neutrophil density shows an increase as oxygen levels decrease and peaks at $Ox = 0.38$, before starting to decrease as oxygen is further reduced.

The analysis illustrated in Fig. 3.2 is based on the baseline parameters introduced in the Methods section. We now investigate the sensitivity of the parameters involved in this subsystem. In particular, we are interested in the contribution of DAMPs to neutrophil recruitment. As discussed earlier, the parameters were constrained based on literature reports. Accordingly, the recruitment of neutrophils peaks when $\lambda_{n,Da}Hi(Da) + \lambda_{n,KC}Hi(KC) \geq 1$. Our initial guess was simply to give equal contribution to DAMPs and KC, and we chose $\lambda_{n,Da} = \lambda_{n,KC} = 0.5$. In Fig. 3.3 we vary at the relative weights by changing $\lambda_{n,Da}$. The effect of varying $\lambda_{n,Da}$ within the interval $[0.3, 0.7]$ on the steady state of keratinocytes and neutrophils is shown in Fig. 3.3a. The higher the influence of DAMPs in neutrophil recruitment, the more pronounced the peak of the neutrophil population becomes. The expected effect on the keratinocyte population is a gradual shift downwards with an increase in neutrophil numbers. However, an interesting feature of the system is that the effect of DAMPs in the steady state seems to be restricted to oxygen levels $Ox < 0.67$. A closer look at the phase space provides a more complete picture. As $\lambda_{n,Da}$ increases, the neutrophil nullcline shows a high nonlinearity and the system could become bistable at high oxygen (Fig. 3.3b). This potential bistability is a function of oxygen. Fig.

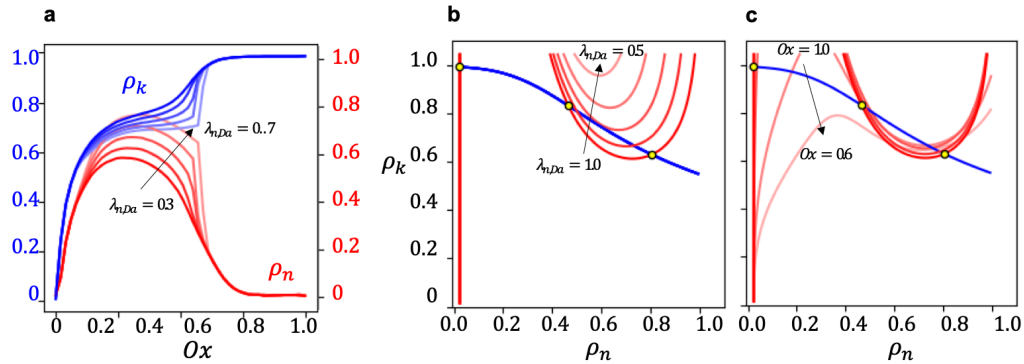


Fig. 3.3. Analysis of the network when the parameter $\lambda_{n,Da}$ is modified. $\lambda_{n,Da}$ controls the recruitment of neutrophils in response to DAMPs from necrotic cells. The baseline value of the parameter was set based on the evidence that the neutrophil population peaks when the combined recruitment signal from hypoxia Kc and damage molecules Da reaches 1. The parameters were originally set to $\lambda_{n,Da} = \lambda_{n,Kc} = 0.5$. a) Varying $\lambda_{n,Da}$ in the range $[0.3, 0.7]$ has a slight effect on the steady state as a function of oxygen. The solution seems to have a very sharp response at $Ox = 0.67$. b) The change in the neutrophil nullcline in the phase-space plot shows that this nullcline intersects the $\dot{\rho}_k$ nullcline at multiple locations and the system could be bistable. c) The intersection of the nullclines is dependent on oxygen concentration; as oxygen decreases, a single stable point is reached at $Ox = 0.67$.

3.3c shows that as oxygen decreases, the system eventually reaches a single stable point. It is unclear if this behavior is actually observed in a typical ulcer, yet, it underscores the sensitivity of the system to this particular feedback element.

Fig. 3.4 shows the sensitivity analysis for the parameters $\lambda_{n,Kc}$ and $\lambda_{k,Ta}$. The parameter $\lambda_{n,Kc}$ enters the Hill function $Hi(Kc)$ in Eq. (3.3), and controls the sensitivity of neutrophils to the KC signal produced by keratinocytes. Consequently, an increase in this parameter leads to an increase in the neutrophil numbers. The keratinocytes are indirectly affected by this parameter, showing a decrease with larger neutrophil values. The parameter $\lambda_{n,Kc}$ enters the Hill function $Hi(Ta)$ in Eq. (3.1), and controls the necrosis rate of keratinocytes in response to $TNF\alpha$. An increase

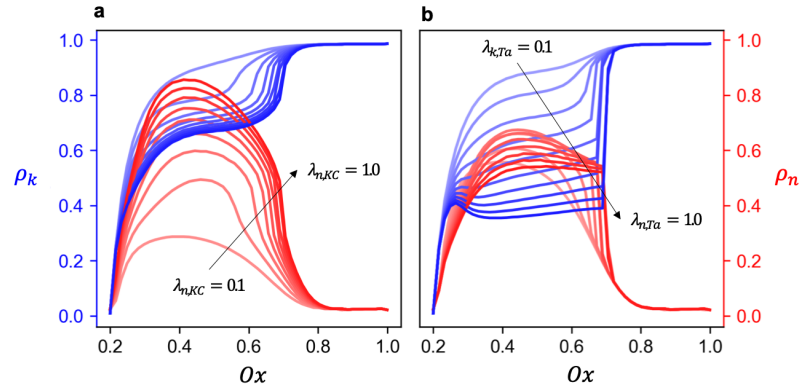


Fig. 3.4. a) Analysis of the circuit when the parameter $\lambda_{n,KC}$ is modified. This parameter controls the sensitivity of neutrophils to the KC signal produced by keratinocytes in response to hypoxia. An increase $\lambda_{n,KC}$ is thus reflected in higher values of ρ_n . b) Analysis of the circuit when the parameter $\lambda_{k,Ta}$ is modified. This parameter controls the necrosis of keratinocytes and is produced by infiltrating neutrophils. Increasing this parameter leads to a decrease in keratinocyte viability, i.e. a shift towards lower values for the ρ_k curves.

in $\lambda_{n,KC}$ thus leads to a drastic reduction in keratinocyte viability with decreasing oxygen.

3.3.2 Pressure Ulcer Formation at the Tissue Scale

Fig. 3.5 summarizes the results of the tissue scale model with the baseline parameters described in the Methods section. All contour plots correspond to the steady state response for the two cell types considered and four of the chemical species. Three values of applied pressure are considered: 0, 25 and 50 kPa.

Fig. 3.5a shows the concentration contours of the normalized oxygen concentrations as the applied pressure in the center of the domain increases. When no pressure is applied, we recover the physiological oxygen concentration: the entire domain is normoxic with $Ox = 1$. Only the region at the center of domain, which is not in contact with the atmosphere, shows a negligible drop in oxygen. The middle con-

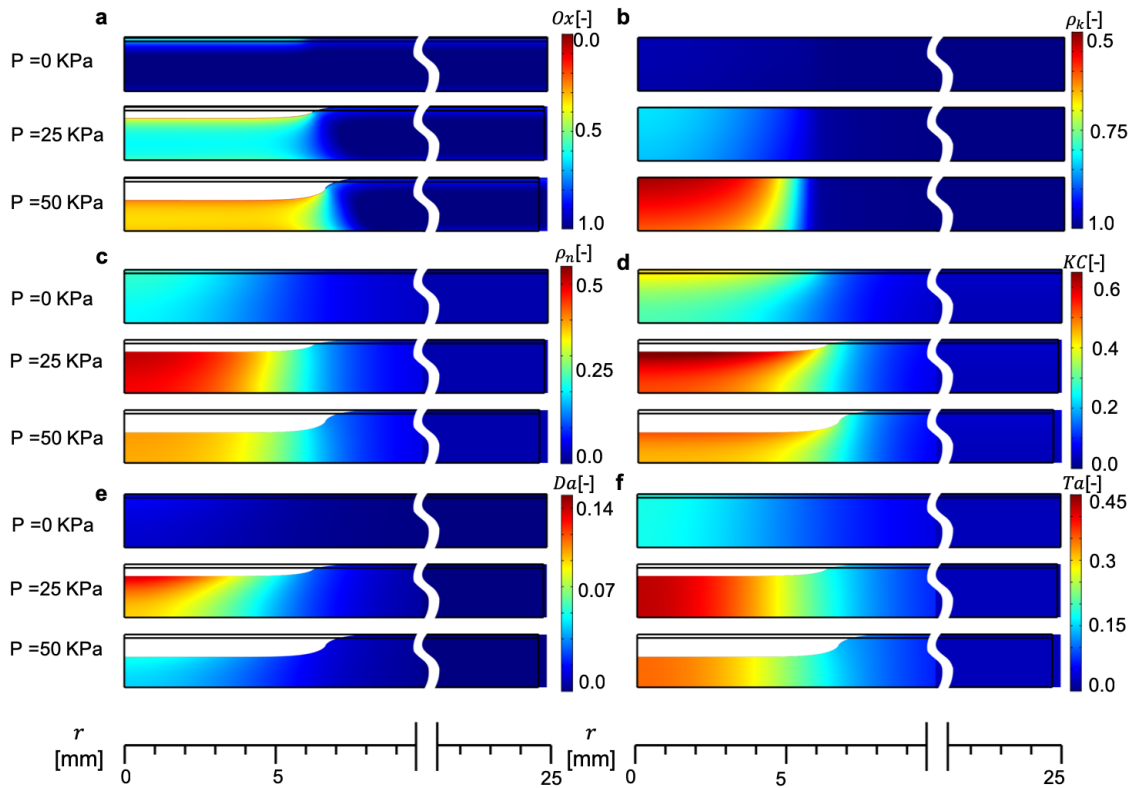


Fig. 3.5. Steady state contours of oxygen, cell species and cytokines as a function of applied pressure. a) Oxygen shows a physiological, uniform normoxic state of $Ox = 1$ at zero pressure. Increasing the load compresses the tissue, reduces the oxygen source term, and leads to hypoxia contours. b) Keratinocyte density, depicted only in the epidermis, decreases with increasing applied load. c) Neutrophil normalized density initially increases with larger applied pressure, but at $P=50$ KPa the neutrophil density is smaller compared to the intermediate loading. d) KC production is proportional to both hypoxia and keratinocyte density, hence, it is maximum at intermediate pressure loading. e) DAMPS are produced by keratinocytes as they necrose under the effect of inflammatory signals, showing the most heterogeneous response of all cytokines. DAMPS are higher at the center of the domain and gradually decrease towards the edge of the compressed zone. f) $TNF\alpha$ contours mirror those of neutrophil density.

tour in Fig. 3.5a corresponds to a load of 25kPa. Deformation of the center-domain leads to a compression-induced reduction in the oxygen source term. Accordingly,

the center of the domain shows a drop in oxygen concentration. Previous experimental studies on trans-cutaneous oxygen tension measurements in skin have predicted a similar decrease in oxygen availability in response to pressure load [11]. As the pressure is increased, the oxygen concentration drops even further. At an applied pressure of 50kPa, the normalized oxygen concentration variable drops to 0.25 within the epidermis, implying that keratinocytes are subjected to severe hypoxic conditions.

The contours of the normalized keratinocyte density are depicted in Fig. 3.5b. In the physiological state $\rho_k = 1$ as expected. When the pressure load reaches 25kPa, a decrease in keratinocyte viability can be observed. However, the reduction is not dramatic. This should be contrasted to the corresponding profile of neutrophil density shown in Fig. 3.5b. Neutrophil values reach peak levels of $\rho_n = 0.5$ at the center of the compressed tissue at 25kPa. This behavior of the system is consistent with the previous analysis of the ODE. As the oxygen decreases, keratinocytes sense the hypoxic condition and release pro-inflammatory chemokines, even if the oxygen levels are not yet low enough to impair keratinocyte function. The strength of the nonlinear feedback between keratinocytes and neutrophils could affect this trend, as seen in the sensitivity analysis of Figs. 3.2 and 3.3. With the baseline parameters, however, a greater pressure is needed to observe a significant reduction in the keratinocyte population. At an applied pressure of 50kPa, the keratinocyte population density drops to a normalized value of 0.5, implying impending tissue necrosis and wound formation. At this load, in contrast, the neutrophil contours are of lower magnitude compared to the intermediate loading.

The keratinocyte and neutrophil normalized densities are better understood by looking at the contours of the chemical species shown in Fig. 3.5d-f. The keratinocyte chemokine (KC) contours of Fig.3.5d confirm that keratinocytes produce this signal at moderate hypoxic conditions. As keratinocyte numbers drop, the KC signal also drops, even if hypoxia becomes more severe. The profile of the damage variable DAMPS (Da) in Fig.3.5e is more interesting. While for the two cell types it appears as if the entire region under compression shows the same response, DAMPS contours,

particularly at an applied pressure of 25kPa, show that this is not the case. At the center of the axisymmetric domain the value of DAMPS is maximum with $Da = 0.14$, and this value decreases to $Da = 0$ towards the end of the loaded region.

Since chemical signals and cells obey diffusive transport, we can expect length scale effects in their steady state values. To investigate this assumption, we continuously vary the size of the region in which the pressure load is applied, as well as the value of the applied pressure. Fig. 3.6a-b illustrates the keratinocyte and neutrophil densities as the radius of the compressed zone, R_{disk} , is changed at a constant pressure of 50 kPa for keratinocytes and 25kPa for neutrophils. It is immediately clear that increasing the pressurized zone results in a decrease of keratinocyte density as well as higher peak neutrophil density, indicating exacerbated wound formation. This is an important difference with respect to the analysis of the ODE system, in which spatial phenomena are not accounted for. It should also be noted that while there is variation of ρ_k and ρ_n along the radial direction, for the largest compressed zone, $r \in [0, 10]$ mm, this variation occurs over a small region $r \in [7, 10]$ mm.

For a more complete picture we plot the average concentration of each variables of interest as a function of both the size of the compressed zone and the magnitude of the applied pressure (Fig.3.6c). The worsening of the ulcer, measured as a decrease of keratinocyte density, is proportional to both the size of the compressed zone and the pressure magnitude. Yet, this relationship is nonlinear, with greater sensitivity to applied pressure for larger zones of compression. Neutrophil density curves show that for small zones of compression increasing the pressure leads to an almost monotonic increase in ρ_n . However, as the pressure disk radius increases, the ρ_n curves recover the concave shape seen in Fig. 3.3.

Another interesting observation is that the average curves of cell population density in Fig.3.6c converge to a single curve as the pressure disk radius increases, indicating that beyond a certain limit the diffusive transport effects do not influence the cell densities. This also applies to the other chemical species plotted in Fig.3.6c. Yet, not all variables seem to converge to this limiting behavior at the same rate. For example

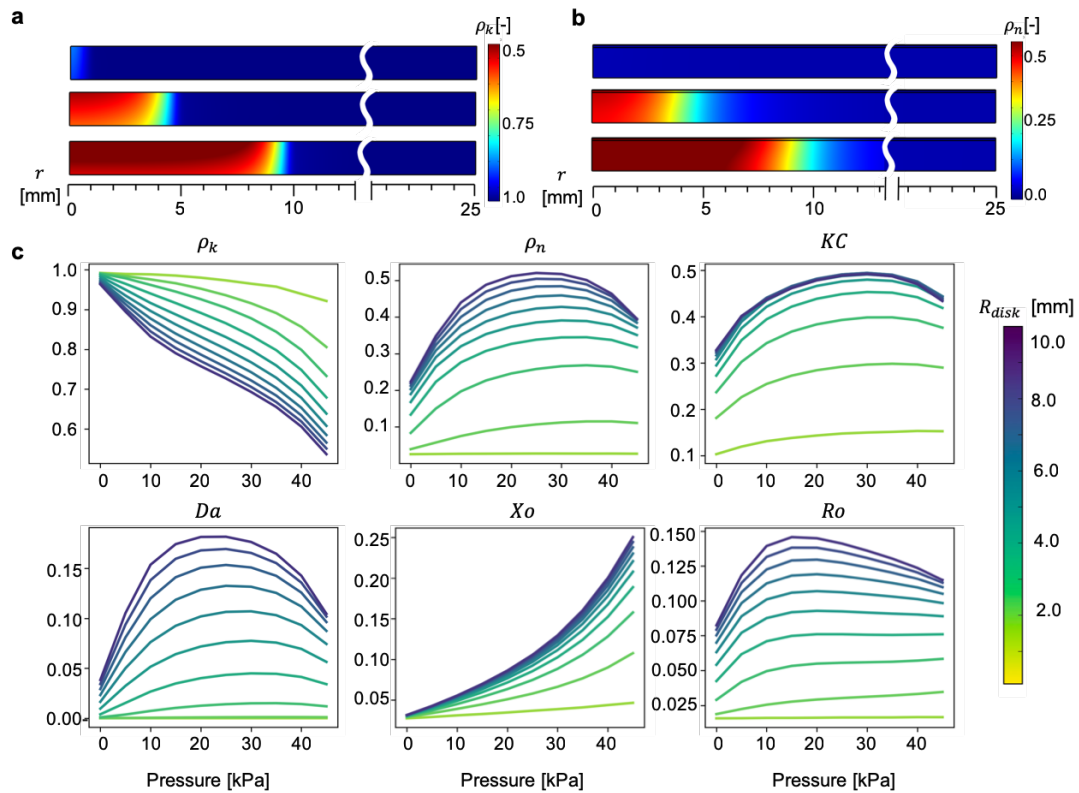


Fig. 3.6. Effect of changing the pressure magnitude and the radius of the compressed zone R_{disk} . a) Contours of the keratinocyte density in the epidermis as the compressed zone radius takes the values $R_{disk} = 1, 5, 10$ mm. Increasing the size of the pressure disk leads to a decrease in ρ_k , however, for $R_{disk} = 10$ mm, the values of ρ_k stay relatively constant for $r \in [0, 7]$ mm and the spatial variation is mostly constrained to the range $r \in [7, 10]$ mm. b) Contours of neutrophil density over the entire domain as the compressed zone radius takes the values $R_{disk} = 1, 5, 10$ mm. c) Average values of the different variables of interest obtained by integrating the contours in the part of the domain under compression. Keratinocyte density monotonically decreases with an increase in both pressure magnitude and pressure disk size. The curves converge to a limiting behavior. Neutrophil density curves show lower sensitivity to the pressure magnitude for smaller R_{disk} . As the R_{disk} increases, a neutrophil curve similar the 0D analysis is recovered.

it is clear that by applying pressure to a zone of $R_{disk} = 10\text{mm}$, the KC response has collapsed to a curve. In the case of DAMPS (Da), even at $R_{disk} = 10\text{mm}$, this is not yet the case. We explain these trends based on the structure of the signaling network. While KC is a signal that depends solely on the oxygen and keratinocyte concentrations, DAMPs levels result from the interaction of ρ_k , Ro , and Ta . As a consequence of being downstream in the regulatory network, the response of Da is less responsive to the change in the pressure disk size.

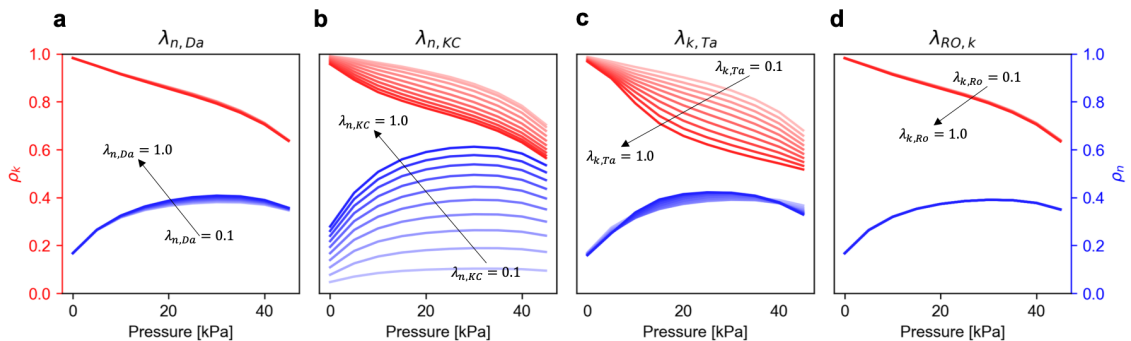


Fig. 3.7. Sensitivity of the average keratinocyte, ρ_k , and neutrophil, ρ_n , densities obtained from integration over the tissue scale domain to the Hill function parameters. a) Neither the keratinocyte nor the neutrophil densities are affected by the DAMPs parameter $\lambda_{n, Da}$ in the tissue scale model. b) The neutrophil density is highly sensitive to the $\lambda_{n, KC}$ parameter, which controls the response to the KC signal produced by keratinocytes in response to hypoxia. c) The keratinocyte population density is sensitive to the $\lambda_{k, Ta}$ parameter, which controls keratinocyte necrosis in response to $TNF\alpha$ produced by neutrophils. d) Neither of the cell populations is sensitive to the parameter associated to the ROS variable.

Following the sensitivity analysis of Fig. 3.2, we perform a similar study for the tissue scale model. Fig. 3.7 shows the variation in the steady state values of keratinocytes and neutrophils as each of the λ_x parameters, controlling the interaction terms, are varied while holding all other values constant. Remarkably, the neutrophil population is only sensitive to the variation of $\lambda_{n, KC}$ and not to $\lambda_{n, Da}$. This re-

veals that in the tissue scale model, it is the coupling of applied pressure to oxygen concentration at the epidermis that has the largest effect on ulcer susceptibility.

In contrast, the keratinocyte population is highly sensitive to the action of $\text{TNF}\alpha$, parameterized by $\lambda_{k,Ta}$. Recall that $\text{TNF}\alpha$ is directly responsible for necrosis of keratinocytes. This is in agreement with the sensitivity analysis of the 0D model in Fig. 3.4. The steady state value of keratinocyte density is insensitive to the change $\lambda_{k,Ro}$, which is expected since this parameter is relevant only for the ischemia reperfusion injury which is not captured here. In summary, the regulatory network is largely controlled by the strength of the interaction between the different cells and cytokines, which is achieved by the choice of the λ_x parameters, in particular $\lambda_{k,Ta}$ and $\lambda_{n,KC}$.

4. CONCLUSIONS, DISCUSSION AND FUTURE WORK

The purpose of this study was to advance the current understanding on the formation of pressure ulcers (PUs) by developing a comprehensive mathematical model across different length scales that captures the mechanisms involved in the initiation of pressure injury on skin. To this regard in the first part of the thesis we developed a model of ischemia in skin resulting from applied external pressure and in the second part we developed mathematical description of the systems biology of wound formation by outlining a cell regulatory network and demonstrated how we can link both models in order to create realistic simulations of PU formation and thereby advancing the current understanding in the field.

In chapter 2 we present a multiscale model to link vasculature collapse at the microscopic scale with oxygen diffusion at the tissue scale. The current understanding of pressure ulcers points to pressure driven ischemia as the key factor in ulcer initiation [6]. However, our understanding of this process is limited due to the difficulty in imaging the microvasculature *in vivo* in relevant clinical settings [8, 52]. Therefore, to get a better understanding of how applied pressure can lead to ischemia and, subsequently, to hypoxia, and to use this knowledge in the prevention and treatment of pressure ulcers, we need predictive models. Here we show the first numerical investigation of how applied pressure can lead to deformation and collapse of realistic three-dimensional microvascular trees of the skin, and how the collapse of blood vessels at the microscopic scale can be linked to hypoxia at the tissue level. While a careful calibration of our model is still needed, the geometries and material properties we use are based on reports of the vascular anatomy and mechanical behavior of skin available in the literature [14, 64]. Therefore, we are confident that our investigation is properly contextualized in the current knowledge, and that it paves the way for future experiments to calibrate and test the predictions of our model. This work also sets

a foundation for more sophisticated models that can address unsettled questions of how non-behavioral changes with aging can lead to a higher susceptibility to pressure ulcers in the older adult population.

Previous work on *ex vivo* imaging of the vasculature allowed us to generate realistic RVEs representative of the skin [12–14]. We then used these geometries to study how realistic deformations of the skin can lead to microvasculature collapse and subsequent tissue hypoxia. Our work is not without limitations. In the RVE simulations we ignored a detailed coupling of the solid matrix with the fluid flow inside of the blood vessels. Even though we did not consider the blood flow problem, we anticipated that the presence of fluid in the vasculature would lead to a pressure boundary condition at the vessel walls for the equilibrium problem of the solid matrix. Yet, we kept this pressure constant at 20mmHg. A clear direction for future research is to include the fluid domain and solve the coupled fluid-structure interaction problem [99]. This consideration is likely to affect our oxygen diffusion problem at the tissue scale, since it would allow us to directly relate the oxygen source term to the blood flow prediction, similar to other modeling efforts focused on blood flow and oxygen transport [100]. Additionally, there are other features of tissue perfusion that we ignore, such as the active control of the vasculature to regulate blood flow, especially in response to externally applied pressure [101]. Our current approach links the oxygen source term to the volume fraction of the vasculature. This assumption is a simplification of the system compared to the consideration of blood flow, but it is still a reasonable starting point to elucidate the mechanisms of pressure-driven ischemia operating at the microscale.

Compression and shear simulations of the RVE led to insightful results. A key observation based on our simulations is that even though we generated random RVEs, each with a unique vessel tree and slightly different volume fraction in the reference configuration, all the curves of vessel volume change against RVE strains collapsed into a single normalized volume fraction response. It remains to explore this phenomenon further in order to uncover the microscale characteristics that dictate the

trends seen in the normalized volume fraction curves. One limitation in our approach is that the RVEs were generated based on reports of the vascular anatomy of adults [12,14]. Further work is needed to incorporate changes in vasculature anatomy with aging [102]. For example, it has been reported that the vasculature in older adults is less dense compared to a younger population [103]. Our study shows that, for the range of volume fractions considered, the initial volume fraction has no influence on the normalized volume fraction changes under applied RVE deformation. However, more work is needed to know if this trend remains true for less dense networks. It is also needed to characterize the baseline level of oxygen perfusion in the older adult population and compare it to the adult population [104]. Other changes in vasculature anatomy with age, and not just volume fraction, may also contribute to a different microvasculature deformation pattern.

Another key result of our simulations is that pure shear does not result in a significant reduction of blood vessel volume fraction. This observation might be a consequence of the distinctive geometric features of the vascular tree. A future direction is to isolate the geometric features of the tree that are predictive of the cross section changes of individual vessels. Our result raises some questions about the importance of simple shear in the development of pressure ulcers. The role of shear deformations on tissue damage has been discussed before [65]. Therefore, it is possible that shear can still be crucial in the development of ulcers. Yet, additional experimental work is needed to validate our predictions that compression of the skin in the thickness direction is the primary mechanism of pressure driven ischemia. Additionally, here we focus on either compression or simple shear of the RVE, yet, a more realistic setup that we are currently pursuing is to subject the RVEs to arbitrary deformations and use data-driven modeling techniques to learn the corresponding microvasculature deformation response [105]. This extension of the RVE predictions might become more important for arbitrary tissue-scale geometries.

Our multiscale model reveals that the relationship between applied pressure and hypoxia at the tissue level is highly nonlinear. From the results of the RVE deformation

we first see that normal strains of 20 percent cause more than a 40 percent drop in the normalized volume fraction of the vasculature. This first relationship, at the RVE level, is only slightly nonlinear as can be seen in Figure 2.9b. However, connecting these results to a tissue-level model of oxygen diffusion we are then able to connect applied pressure at the skin outer surface to the oxygen concentration through the skin thickness. The corresponding plot (Figure 2.10c) shows that the coupling of the different physical phenomena across scales increases the nonlinearity and sensitivity of the variable of interest, the oxygen concentration in the skin. In fact, the results indicate that the application of a 50kPa pressure, which is not uncommon [106, 107], produces a drop of more than 50 percent in oxygen compared to the physiological regime. This level of hypoxia has been shown to hinder the growth rate of native skin cells and collagen deposition in *in vitro* experiments [108,109]. A more thorough calibration is of course needed. For instance, we assumed that the oxygen source term is linearly related to the normalized volume fraction of blood in the dermis. The model can be improved, as mentioned before, by accounting for blood flow and transport between the blood circulating in the microvasculature and the surrounding tissue [100]. This type of endeavor is beyond the scope of this manuscript. Nevertheless, even with the simplified connection between microvasculature deformation and oxygen supply, our simulations yield results consistent with the current understanding of pressure-driven ischemia and ulcer formation.

One of the primary motivations for developing the current model is that it enables the simulation of pressure-driven hypoxia for arbitrary domains. Here we show a relatively simple domain for the tissue-level simulations. However, the problem can be easily extended to more realistic settings. With our axisymmetric domain we show that the oxygen concentration contours have a characteristic geometry. The region where hypoxia is more evident is right underneath the surface of the epidermis where the load is applied. The oxygen contours are not constant through the thickness but rather show an hourglass-shaped hypoxic region for the baseline thickness and material properties considered. Finally, one more advantage of the tissue-level model

is the ability to investigate *in silico* how changes in skin anatomy and mechanical behavior can be linked to corresponding changes in pressure-driven hypoxia. Recent studies in mice show that skin's strain-stress response shifts toward larger strains, i.e. the tissue is more compliant at moderate stresses [110]. Here we show that the oxygen contours are very sensitive to a reduction in skin stiffness, possibly explaining one factor involved in the greater susceptibility to pressure ulcer initiation with age. We also know that skin changes in thickness as we grow older, becoming thinner [111]. Incorporating this knowledge into our model we find that the effect of dermis thinning with respect to our baseline does not result in a dramatic change in the oxygen concentration profile under applied pressure. Interestingly, a recent study in mice suggests that older but obese mice may be at less risk to ulcer initiation due to the increased thickness of their skin [112]. In alignment with this hypothesis, we predict that the pressure-driven ischemic response is sensitive to an increase in thickness with respect to our baseline.

In chapter 2, we present a multiscale model that predicts hypoxia contours at the tissue level based on a microscale model of microvascular collapse. We use parameters and geometries for the mechanical behavior of skin and microvasculature characteristics reported in the literature. The model predicts oxygen concentration contours indicative of tissue hypoxia when moderate levels of pressure are applied at the skin outer surface. The predictions are in good agreement with existing knowledge of pressure-driven ischemia. Our model enabled us to explore for the first time how changes in skin with aging might affect the increased susceptibility to pressure induced ischemia in the older adult population. Therefore, we expect that future work will allow us to further calibrate and validate the model, and lead to the development of better prevention and treatment tools for pressure ulcers that incorporate age-specific changes in skin anatomy and mechanical properties.

Having studied the initiating factor of PU formation, the pressure induced ischemia in skin, in chapter 3 a detailed analysis of the regulatory network implicated in pressure ulcer (PU) formation and its implementation into a tissue scale finite

element model of skin mechanics and oxygen diffusion is presented. In contrast to recent mathematical descriptions of PUs as agent-based models, we opt to describe the system with a set of ODEs. Agent-based models are convenient to explore emergent behavior stemming from simple rules and discrete entities, but are not easily adapted to large spatial scales and arbitrary spatial domains. In contrast, an ODE description of a signaling network lends itself to spatial extensions that naturally capture the temporo-spatial evolution of the different variables in realistic domains. Moreover, it allows coupling to other crucial phenomena such as pressure-driven ischemia. Additionally, the ODE approach provides access to mathematical tools that allow exploring the relative contribution of each of the elements to the overall system behavior and to perform sensitivity analyses of the parameters. Thus, we expect that this model will be useful to interpret new experimental data, and to develop enhanced models that build upon the work shown here.

The starting point to our model in Chapter 3 is a comprehensive regulatory network of PU biology which has been extensively studied, validated, and analyzed previously [6, 32, 36, 37, 113, 114]. In a first approximation, we focused on a subset of the network: the keratinocyte-neutrophil subsystem. In future work, we will extend our work to more comprehensive model that will also incorporate the different macrophage populations, especially the M1 population which is assumed to drive the unrestrained inflammation seen in chronic wounds and pressure ulcers [115]. By restricting our attention to the neutrophil infiltration we capture the initial sterile inflammation response that characterizes the early stages in pressure ulcer formation [85, 86, 88].

Given the topology of the regulatory system, a major modeling question is how to represent mathematically the dynamics of each element and the interactions between the elements. We use logistic growth equations for the cells, and the interaction terms are modeled with Hill functions, which is a standard approach in computational systems biology [74, 75]. The most important degrees of freedom of the model are precisely the parameters of the Hill functions controlling the interaction strength and

sensitivity between the network elements. This is a significant assumption, and more research is needed to validate that the model can replicate the overall dynamics of more comprehensive, first-principle models [76]. At the same time, by reducing the system to the key elements and introducing the essential coupling terms we expect to truly capture the distinctive features of the early pressure ulcer formation events.

While we do not calibrate our mathematical model to a full set of data, we do narrow down the parameters based on reliable literature data and explore the sensitivity of system to changes in these parameters. Based on these literature data and sensitivity studies, we are able to capture important features of PU formation such as the nonlinear feedback between release of pro-inflammatory signals by keratinocytes under hypoxia and neutrophil-driven necrosis mediated by $\text{TNF}\alpha$. The system shows that as the oxygen is decreased, the nonlinear feedback induces a sharp increase in neutrophil infiltration. However, in the absence of other mechanisms of inflammation, the reduction in the keratinocyte population is mild for intermediate oxygen values, and it only drops to low numbers if hypoxia is extreme, i.e. oxygen concentrations below 20% of physiological values. This result further suggests that other steps in the inflammation cascade, in particular the dynamics of M1 and M2 macrophages, are needed to capture the later stages of ulcer progression [116–118].

Unarguably, our most important contribution comes from the extension of the inflammation regulatory network to the tissue scale domain, including its coupling to the tissue mechanics and oxygen diffusion. Previous work on PU modeling has emphasized the features of the biological signaling cascade [36]. Our approach emphasizes the role of pressure-driven ischemia and subsequent hypoxia as a key mechanism in PU formation. In the tissue scale model, the parameter sensitivity analysis reveals that the ulcer response is most sensitive to the keratinocyte chemoattractant (KC) signal released as a result of hypoxia. Interestingly, the KC signal is controlled by the oxygen profile, which itself is nonlinearly related to the pressure applied to the skin surface. This results underscores the need to better understand how pressure is connected to oxygen concentration profiles in the tissue, especially near the epidermis.

Furthermore, the mechanics of ischemia are especially relevant in the context of aging. There are several risk factors for increased susceptibility to PU in older adults, including a different inflammation response and a more sedentary lifestyle [70, 71]. Nonetheless, it is also recognized that our skin mechanical properties, structure, and microvascular anatomy change markedly with age [72, 102, 111, 119]. Based on our results, we anticipate that taking these factors into account could be critically important to better understand PU initiation and progression in the aging population.

REFERENCES

- [1] C. H. Lyder and E. A. Ayello, "Pressure ulcers: a patient safety issue," 2008.
- [2] L. Demarré, A. Van Lancker, A. Van Hecke, S. Verhaeghe, M. Grypdonck, J. Lemey, L. Annemans, and D. Beeckman, "The cost of prevention and treatment of pressure ulcers: a systematic review," *International journal of nursing studies*, vol. 52, no. 11, pp. 1754–1774, 2015.
- [3] M. Kosiak, "Etiology of decubitus ulcers." *Archives of physical medicine and rehabilitation*, vol. 42, p. 19, 1961.
- [4] D. Gawlitta, C. W. Oomens, D. L. Bader, F. P. Baaijens, and C. V. Bouten, "Temporal differences in the influence of ischemic factors and deformation on the metabolism of engineered skeletal muscle," *Journal of Applied Physiology*, vol. 103, no. 2, pp. 464–473, 2007.
- [5] F. Liao, S. Burns, and Y.-K. Jan, "Skin blood flow dynamics and its role in pressure ulcers," *Journal of tissue viability*, vol. 22, no. 2, pp. 25–36, 2013.
- [6] S. Coleman, J. Nixon, J. Keen, L. Wilson, E. McGinnis, C. Dealey, N. Stubbs, A. Farrin, D. Dowding, J. M. Schols *et al.*, "A new pressure ulcer conceptual framework," *Journal of advanced nursing*, vol. 70, no. 10, pp. 2222–2234, 2014.
- [7] C. Dealey, C. T. Brindle, J. Black, P. Alves, N. Santamaria, E. Call, and M. Clark, "Challenges in pressure ulcer prevention," *International wound journal*, vol. 12, no. 3, pp. 309–312, 2015.
- [8] O. Timar-Banu, H. Beauregard, J. Tousignant, M. Lassonde, P. Harris, G. Viau, L. Vachon, E. Levy, and T. Abribat, "Development of noninvasive and quantitative methodologies for the assessment of chronic ulcers and scars in humans," *Wound Repair and Regeneration*, vol. 9, no. 2, pp. 123–132, 2001.
- [9] A. A. Manorama, S. Baek, J. Vorro, A. Sikorskii, and T. R. Bush, "Blood perfusion and transcutaneous oxygen level characterizations in human skin with changes in normal and shear loadsimplications for pressure ulcer formation," *Clinical biomechanics*, vol. 25, no. 8, pp. 823–828, 2010.
- [10] S. M. Peirce, T. C. Skalak, and G. T. Rodeheaver, "Ischemia-reperfusion injury in chronic pressure ulcer formation: a skin model in the rat," *Wound repair and regeneration*, vol. 8, no. 1, pp. 68–76, 2000.
- [11] D. Colin and J. Saumet, "Influence of external pressure on transcutaneous oxygen tension and laser doppler flowmetry on sacral skin," *Clinical Physiology*, vol. 16, no. 1, pp. 61–72, 1996.

- [12] I. M. Braverman, “Ultrastructure and organization of the cutaneous microvasculature in normal and pathologic states,” *Journal of Investigative Dermatology*, vol. 93, no. 2, pp. S2–S9, 1989.
- [13] I. M. Braverman, A. Keh, and D. Goldminz, “Correlation of laser doppler wave patterns with underlying microvascular anatomy,” *Journal of Investigative Dermatology*, vol. 95, no. 3, pp. 283–286, 1990.
- [14] G. Cevc and U. Vierl, “Spatial distribution of cutaneous microvasculature and local drug clearance after drug application on the skin,” *Journal of controlled release*, vol. 118, no. 1, pp. 18–26, 2007.
- [15] L.-C. Gerhardt, J. Schmidt, J. Sanz-Herrera, F. Baaijens, T. Ansari, G. Peters, and C. Oomens, “A novel method for visualising and quantifying through-plane skin layer deformations,” *Journal of the mechanical behavior of biomedical materials*, vol. 14, pp. 199–207, 2012.
- [16] B. Müller, J. Elrod, M. Pensalfini, R. Hopf, O. Distler, C. Schiestl, and E. Mazza, “A novel ultra-light suction device for mechanical characterization of skin,” *PloS one*, vol. 13, no. 8, p. e0201440, 2018.
- [17] Z. Sadler, J. Scott, J. Drost, S. Chen, S. Roccabianca, and T. R. Bush, “Initial estimation of the in vivo material properties of the seated human buttocks and thighs,” *International Journal of Non-Linear Mechanics*, vol. 107, pp. 77–85, 2018.
- [18] N. Mitchell, E. Sifakis *et al.*, “Gridiron: An interactive authoring and cognitive training foundation for reconstructive plastic surgery procedures,” *ACM Transactions on Graphics (TOG)*, vol. 34, no. 4, p. 43, 2015.
- [19] A. B. Tepole, “Computational systems mechanobiology of wound healing,” *Computer Methods in Applied Mechanics and Engineering*, vol. 314, pp. 46–70, 2017.
- [20] T. Lee, A. K. Gosain, I. Billionis, and A. B. Tepole, “Predicting the effect of aging and defect size on the stress profiles of skin from advancement, rotation and transposition flap surgeries,” *Journal of the Mechanics and Physics of Solids*, 2019.
- [21] N. Kumaraswamy, H. Khatam, G. P. Reece, M. C. Fingeret, M. K. Markey, and K. Ravi-Chandar, “Mechanical response of human female breast skin under uniaxial stretching,” *Journal of the mechanical behavior of biomedical materials*, vol. 74, pp. 164–175, 2017.
- [22] O. Lokshin and Y. Lanir, “Viscoelasticity and preconditioning of rat skin under uniaxial stretch: microstructural constitutive characterization,” *Journal of biomechanical engineering*, vol. 131, no. 3, p. 031009, 2009.
- [23] J. Weickenmeier, M. Jabareen, and E. Mazza, “Suction based mechanical characterization of superficial facial soft tissues,” *Journal of biomechanics*, vol. 48, no. 16, pp. 4279–4286, 2015.
- [24] G. Limbert, “Mathematical and computational modelling of skin biophysics: a review,” *Proceedings of the Royal Society A: Mathematical, Physical and Engineering Sciences*, vol. 473, no. 2203, p. 20170257, 2017.

- [25] T. Lee, S. Y. Turin, A. K. Gosain, and A. B. Tepole, “Multi-view stereo in the operating room allows prediction of healing complications in a patient-specific model of reconstructive surgery,” *Journal of biomechanics*, vol. 74, pp. 202–206, 2018.
- [26] J. W. Jor, M. D. Parker, A. J. Taberner, M. P. Nash, and P. M. Nielsen, “Computational and experimental characterization of skin mechanics: identifying current challenges and future directions,” *Wiley Interdisciplinary Reviews: Systems Biology and Medicine*, vol. 5, no. 5, pp. 539–556, 2013.
- [27] C. Oomens, D. Van Campen, and H. Grootenboer, “A mixture approach to the mechanics of skin,” *Journal of biomechanics*, vol. 20, no. 9, pp. 877–885, 1987.
- [28] W. Vankan, J. Huyghe, J. Janssen, A. Huson, W. Hacking, and W. Schreiner, “Finite element analysis of blood flow through biological tissue,” *International Journal of Engineering Science*, vol. 35, no. 4, pp. 375–385, 1997.
- [29] E. Linder-Ganz and A. Gefen, “The effects of pressure and shear on capillary closure in the microstructure of skeletal muscles,” *Annals of biomedical engineering*, vol. 35, no. 12, pp. 2095–2107, 2007.
- [30] M. Shilo and A. Gefen, “Identification of capillary blood pressure levels at which capillary collapse is likely in a tissue subjected to large compressive and shear deformations,” *Computer methods in biomechanics and biomedical engineering*, vol. 15, no. 1, pp. 59–71, 2012.
- [31] Y. Saito, M. Hasegawa, M. Fujimoto, T. Matsushita, M. Horikawa, M. Takenaka, F. Ogawa, J. Sugama, D. A. Steeber, S. Sato *et al.*, “The loss of mcp-1 attenuates cutaneous ischemia–reperfusion injury in a mouse model of pressure ulcer,” *Journal of Investigative Dermatology*, vol. 128, no. 7, pp. 1838–1851, 2008.
- [32] S. A. Eming, P. Martin, and M. Tomic-Canic, “Wound repair and regeneration: mechanisms, signaling, and translation,” *Science translational medicine*, vol. 6, no. 265, pp. 265sr6–265sr6, 2014.
- [33] M. Valko, D. Leibfritz, J. Moncol, M. T. Cronin, M. Mazur, and J. Telser, “Free radicals and antioxidants in normal physiological functions and human disease,” *The international journal of biochemistry & cell biology*, vol. 39, no. 1, pp. 44–84, 2007.
- [34] R. Anderson, K. Patel, K. Reghebi, and S. Hill, “Conversion of xanthine dehydrogenase to xanthine oxidase as a possible marker for hypoxia in tumours and normal tissues,” *British journal of cancer*, vol. 60, no. 2, p. 193, 1989.
- [35] S. L. Linas, D. Whittenburg, and J. E. Repine, “Role of xanthine oxidase in ischemia/reperfusion injury,” *American Journal of Physiology-Renal Physiology*, vol. 258, no. 3, pp. F711–F716, 1990.
- [36] C. Ziraldo, A. Solovyev, A. Allegretti, S. Krishnan, M. K. Henzel, G. A. Sowa, D. Brienza, G. An, Q. Mi, and Y. Vodovotz, “A computational, tissue-realistic model of pressure ulcer formation in individuals with spinal cord injury,” *PLoS computational biology*, vol. 11, no. 6, p. e1004309, 2015.

- [37] S. Nagaraja, A. Wallqvist, J. Reifman, and A. Y. Mitrophanov, “Computational approach to characterize causative factors and molecular indicators of chronic wound inflammation,” *The Journal of Immunology*, vol. 192, no. 4, pp. 1824–1834, 2014.
- [38] F. Hendriks, D. Brokken, C. Oomens, D. Bader, and F. Baaijens, “The relative contributions of different skin layers to the mechanical behavior of human skin in vivo using suction experiments,” *Medical engineering & physics*, vol. 28, no. 3, pp. 259–266, 2006.
- [39] C. Paillet-Mattei, S. Bec, and H. Zahouani, “In vivo measurements of the elastic mechanical properties of human skin by indentation tests,” *Medical engineering & physics*, vol. 30, no. 5, pp. 599–606, 2008.
- [40] X. Liu, J. Cleary, and G. German, “The global mechanical properties and multi-scale failure mechanics of heterogeneous human stratum corneum,” *Acta biomaterialia*, vol. 43, pp. 78–87, 2016.
- [41] H. Shimizu, *Shimizu’s textbook of dermatology*. JA KUBU, 2007.
- [42] M. Stücker, A. Struk, P. Altmeyer, M. Herde, H. Baumgärtl, and D. W. Lübbers, “The cutaneous uptake of atmospheric oxygen contributes significantly to the oxygen supply of human dermis and epidermis,” *The Journal of physiology*, vol. 538, no. 3, pp. 985–994, 2002.
- [43] R. B. Groves, S. A. Coulman, J. C. Birchall, and S. L. Evans, “An anisotropic, hyperelastic model for skin: experimental measurements, finite element modelling and identification of parameters for human and murine skin,” *Journal of the mechanical behavior of biomedical materials*, vol. 18, pp. 167–180, 2013.
- [44] M. L. Crichton, B. C. Donose, X. Chen, A. P. Raphael, H. Huang, and M. A. Kendall, “The viscoelastic, hyperelastic and scale dependent behaviour of freshly excised individual skin layers,” *Biomaterials*, vol. 32, no. 20, pp. 4670–4681, 2011.
- [45] D. J. Gould, T. J. Vadakkan, R. A. Poché, and M. E. Dickinson, “Multifractal and lacunarity analysis of microvascular morphology and remodeling,” *Microcirculation*, vol. 18, no. 2, pp. 136–151, 2011.
- [46] G. A. Losa, “Fractals in biology and medicine,” *Reviews in Cell Biology and Molecular Medicine*, 2006.
- [47] B. B. Mandelbrot, “Self-affine fractals and fractal dimension,” *Physica scripta*, vol. 32, no. 4, p. 257, 1985.
- [48] A. L. Goldberger, V. Bhargava, B. J. West, and A. J. Mandell, “On a mechanism of cardiac electrical stability. the fractal hypothesis,” *Biophysical journal*, vol. 48, no. 3, pp. 525–528, 1985.
- [49] M. H. Tawhai, A. Pullan, and P. Hunter, “Generation of an anatomically based three-dimensional model of the conducting airways,” *Annals of biomedical engineering*, vol. 28, no. 7, pp. 793–802, 2000.
- [50] F. S. Costabal, D. E. Hurtado, and E. Kuhl, “Generating purkinje networks in the human heart,” *Journal of biomechanics*, vol. 49, no. 12, pp. 2455–2465, 2016.

- [51] T. Ijiri, T. Ashihara, T. Yamaguchi, K. Takayama, T. Igarashi, T. Shimada, T. Namba, R. Haraguchi, and K. Nakazawa, "A procedural method for modeling the purkinje fibers of the heart," *The journal of physiological sciences*, vol. 58, no. 7, pp. 481–486, 2008.
- [52] W. J. Choi, H. Wang, and R. K. Wang, "Optical coherence tomography microangiography for monitoring the response of vascular perfusion to external pressure on human skin tissue," *Journal of biomedical optics*, vol. 19, no. 5, p. 056003, 2014.
- [53] I. V. Meglinski and S. J. Matcher, "Quantitative assessment of skin layers absorption and skin reflectance spectra simulation in the visible and near-infrared spectral regions," *Physiological measurement*, vol. 23, no. 4, p. 741, 2002.
- [54] G. E. Nilsson, T. Tenland, and P. A. Oberg, "Evaluation of a laser doppler flowmeter for measurement of tissue blood flow," *IEEE Transactions on Biomedical Engineering*, no. 10, pp. 597–604, 1980.
- [55] T. Lister, P. A. Wright, and P. H. Chappell, "Optical properties of human skin," *Journal of biomedical optics*, vol. 17, no. 9, p. 090901, 2012.
- [56] Y. v. H. Juergen Riegel, Werner Mayer, "Freecad (version 0.17.13541)," <http://www.freecadweb.org/>, 2001–2018.
- [57] J. M. Benítez and F. J. Montáns, "The mechanical behavior of skin: Structures and models for the finite element analysis," *Computers & Structures*, vol. 190, pp. 75–107, 2017.
- [58] Y. Lanir, "Constitutive equations for fibrous connective tissues," *Journal of biomechanics*, vol. 16, no. 1, pp. 1–12, 1983.
- [59] G. Limbert, "State-of-the-art constitutive models of skin biomechanics," *Computational Biophysics of the Skin*, p. 558, 2014.
- [60] J. Rausch, MKand Humphrey, "A Computational Model of the Biochemomechanics of an Evolving Occlusive Thrombus," *Journal of Elasticity*, vol. 129, no. 1-2, pp. 125–144, 2017.
- [61] A. Buganza-Tepole, J. P. Steinberg, E. Kuhl, and A. K. Gosain, "Application of finite element modeling to optimize flap design with tissue expansion," *Plastic and reconstructive surgery*, vol. 134, no. 4, p. 785, 2014.
- [62] A. N. Annaidh, K. Bruyere, M. Destrade, M. D. Gilchrist, C. Maurini, M. Otténio, and G. Saccomandi, "Automated estimation of collagen fibre dispersion in the dermis and its contribution to the anisotropic behaviour of skin," *Annals of biomedical engineering*, vol. 40, no. 8, pp. 1666–1678, 2012.
- [63] T. C. Gasser, R. W. Ogden, and G. A. Holzapfel, "Hyperelastic modelling of arterial layers with distributed collagen fibre orientations," *Journal of the royal society interface*, vol. 3, no. 6, pp. 15–35, 2005.
- [64] J. T. Iivarinen, R. K. Korhonen, P. Julkunen, and J. S. Jurvelin, "Experimental and computational analysis of soft tissue stiffness in forearm using a manual indentation device," *Medical engineering & physics*, vol. 33, no. 10, pp. 1245–1253, 2011.

- [65] A. F. Mak, M. Zhang, and E. W. Tam, “Biomechanics of pressure ulcer in body tissues interacting with external forces during locomotion,” *Annual review of biomedical engineering*, vol. 12, pp. 29–53, 2010.
- [66] W. A. Bruls, H. Slaper, J. C. van Der Leun, and L. Berrens, “Transmission of human epidermis and stratum corneum as a function of thickness in the ultraviolet and visible wavelengths,” *Photochemistry and photobiology*, vol. 40, no. 4, pp. 485–494, 1984.
- [67] K. A. Holbrook and G. F. Odland, “Regional differences in the thickness (cell layers) of the human stratum corneum: an ultrastructural analysis,” *Journal of Investigative Dermatology*, vol. 62, no. 4, pp. 415–422, 1974.
- [68] W. Wang, “Oxygen partial pressure in outer layers of skin: simulation using three-dimensional multilayered models,” *Microcirculation*, vol. 12, no. 2, pp. 195–207, 2005.
- [69] U. Grossmann, “Simulation of combined transfer of oxygen and heat through the skin using a capillary-loop model,” *Mathematical Biosciences*, vol. 61, no. 2, pp. 205–236, 1982.
- [70] A. N. Moor, E. Tummel, J. L. Prather, M. Jung, J. J. Lopez, S. Connors, and L. J. Gould, “Consequences of age on ischemic wound healing in rats: altered antioxidant activity and delayed wound closure,” *Age*, vol. 36, no. 2, pp. 733–748, 2014.
- [71] R. M. Allman, P. S. Goode, M. M. Patrick, N. Burst, and A. A. Bartolucci, “Pressure ulcer risk factors among hospitalized patients with activity limitation,” *Jama*, vol. 273, no. 11, pp. 865–870, 1995.
- [72] S. Luebberding, N. Krueger, and M. Kerscher, “Mechanical properties of human skin in vivo: a comparative evaluation in 300 men and women,” *Skin Research and Technology*, vol. 20, no. 2, pp. 127–135, 2014.
- [73] J. Leveque, P. Corcuff, J. d. Rigal, and P. Agache, “In vivo studies of the evolution of physical properties of the human skin with age,” *International journal of dermatology*, vol. 23, no. 5, pp. 322–329, 1984.
- [74] C. Xue, A. Friedman, and C. K. Sen, “A mathematical model of ischemic cutaneous wounds,” *Proceedings of the National Academy of Sciences*, vol. 106, no. 39, pp. 16 782–16 787, 2009.
- [75] S. Nagaraja, L. Chen, J. Zhou, Y. Zhao, D. Fine, L. A. DiPietro, J. Reifman, and A. Y. Mitrophanov, “Predictive analysis of mechanistic triggers and mitigation strategies for pathological scarring in skin wounds,” *The Journal of Immunology*, vol. 198, no. 2, pp. 832–841, 2017.
- [76] G. An, Q. Mi, J. Dutta-Moscato, and Y. Vodovotz, “Agent-based models in translational systems biology,” *Wiley Interdisciplinary Reviews: Systems Biology and Medicine*, vol. 1, no. 2, pp. 159–171, 2009.
- [77] H. J. Wearing and J. A. Sherratt, “Keratinocyte growth factor signalling: a mathematical model of dermal–epidermal interaction in epidermal wound healing,” *Mathematical biosciences*, vol. 165, no. 1, pp. 41–62, 2000.

- [78] T. Takei, C. Rivas-Gotz, C. A. Dellings, J. T. Koo, I. Mills, T. L. McCarthy, M. Centrella, and B. E. Sumpio, "Effect of strain on human keratinocytes in vitro," *Journal of cellular physiology*, vol. 173, no. 1, pp. 64–72, 1997.
- [79] M. A. Ngo, N. N. Sinitsyna, Q. Qin, and R. H. Rice, "Oxygen-dependent differentiation of human keratinocytes," *Journal of Investigative Dermatology*, vol. 127, no. 2, pp. 354–361, 2007.
- [80] T. Banno, A. Gazel, and M. Blumenberg, "Effects of tumor necrosis factor- α (tnf α) in epidermal keratinocytes revealed using global transcriptional profiling," *Journal of Biological Chemistry*, vol. 279, no. 31, pp. 32 633–32 642, 2004.
- [81] R. Rückert, G. Lindner, S. Bulfone-Paus, and R. Paus, "High-dose proinflammatory cytokines induce apoptosis of hair bulb keratinocytes in vivo," *British Journal of Dermatology*, vol. 143, no. 5, pp. 1036–1039, 2000.
- [82] A. Schwarz, R. Bhardwaj, Y. Aragane, K. Mahnke, H. Riemann, D. Metze, T. A. Luger, and T. Schwarz, "Ultraviolet-b-induced apoptosis of keratinocytes: evidence for partial involvement of tumor necrosis factor- α in the formation of sunburn cells," *Journal of Investigative Dermatology*, vol. 104, no. 6, pp. 922–927, 1995.
- [83] P. A. Grange, C. Chéreau, J. Raigneaud, C. Nicco, B. Weill, N. Dupin, and F. Batteux, "Production of superoxide anions by keratinocytes initiates p. acnes-induced inflammation of the skin," *PLoS pathogens*, vol. 5, no. 7, p. e1000527, 2009.
- [84] H. R. Rezvani, F. Mazurier, M. Cario-André, C. Pain, C. Ged, A. Taïeb, and H. de Verneuil, "Protective effects of catalase overexpression on uvb-induced apoptosis in normal human keratinocytes," *Journal of Biological Chemistry*, vol. 281, no. 26, pp. 17 999–18 007, 2006.
- [85] M. B. Grisham, L. A. Hernandez, and D. N. Granger, "Xanthine oxidase and neutrophil infiltration in intestinal ischemia," *American Journal of Physiology-Gastrointestinal and Liver Physiology*, vol. 251, no. 4, pp. G567–G574, 1986.
- [86] C. Summers, S. M. Rankin, A. M. Condliffe, N. Singh, A. M. Peters, and E. R. Chilvers, "Neutrophil kinetics in health and disease," *Trends in immunology*, vol. 31, no. 8, pp. 318–324, 2010.
- [87] J. MacDougall and M. McCabe, "Diffusion coefficient of oxygen through tissues," *Nature*, vol. 215, no. 5106, p. 1173, 1967.
- [88] E. Feiken, J. Rømer, J. Eriksen, and L. R. Lund, "Neutrophils express tumor necrosis factor- α during mouse skin wound healing," *Journal of investigative dermatology*, vol. 105, no. 1, pp. 120–123, 1995.
- [89] G. Y. Chen and G. Nuñez, "Sterile inflammation: sensing and reacting to damage," *Nature Reviews Immunology*, vol. 10, no. 12, p. 826, 2010.
- [90] R. Taylor and T. James, "The role of oxidative stress in the development and persistence of pressure ulcers," in *Pressure ulcer research*. Springer, 2005, pp. 205–232.

- [91] C. K. Sen, “Wound healing essentials: let there be oxygen,” *Wound repair and regeneration*, vol. 17, no. 1, pp. 1–18, 2009.
- [92] D. N. Granger, “Role of xanthine oxidase and granulocytes in ischemia-reperfusion injury,” *American Journal of Physiology-Heart and Circulatory Physiology*, vol. 255, no. 6, pp. H1269–H1275, 1988.
- [93] T. J. James, M. A. Hughes, G. W. Cherry, and R. P. Taylor, “Evidence of oxidative stress in chronic venous ulcers,” *Wound Repair and Regeneration*, vol. 11, no. 3, pp. 172–176, 2003.
- [94] K. A. Holbrook and G. F. Odland, “Regional differences in the thickness (cell layers) of the human stratum corneum: an ultrastructural analysis,” *Journal of Investigative Dermatology*, vol. 62, no. 4, pp. 415–422, 1974.
- [95] A. F. Mak, M. Zhang, and E. W. Tam, “Biomechanics of pressure ulcer in body tissues interacting with external forces during locomotion,” *Annual review of biomedical engineering*, vol. 12, pp. 29–53, 2010.
- [96] G. Pettet, H. Byrne, D. McElwain, and J. Norbury, “A model of wound-healing angiogenesis in soft tissue,” *Mathematical biosciences*, vol. 136, no. 1, pp. 35–63, 1996.
- [97] E. Gaffney, K. Pugh, P. Maini, and F. Arnold, “Investigating a simple model of cutaneous wound healing angiogenesis,” *Journal of mathematical biology*, vol. 45, no. 4, pp. 337–374, 2002.
- [98] C. L. Stokes, D. A. Lauffenburger, and S. K. Williams, “Migration of individual microvessel endothelial cells: stochastic model and parameter measurement,” *Journal of cell science*, vol. 99, no. 2, pp. 419–430, 1991.
- [99] P. Causin and F. Malgaroli, “Mathematical modeling of local perfusion in large distensible microvascular networks,” *Computer Methods in Applied Mechanics and Engineering*, vol. 323, pp. 303–329, 2017.
- [100] P. Causin, G. Guidoboni, F. Malgaroli, R. Sacco, and A. Harris, “Blood flow mechanics and oxygen transport and delivery in the retinal microcirculation: multiscale mathematical modeling and numerical simulation,” *Biomechanics and modeling in mechanobiology*, vol. 15, no. 3, pp. 525–542, 2016.
- [101] W. Pan, J. P. Drost, S. Roccabianca, S. Baek, and T. R. Bush, “A potential tool for the study of venous ulcers: Blood flow responses to load,” *Journal of biomechanical engineering*, vol. 140, no. 3, p. 031009, 2018.
- [102] I. Bentov and M. J. Reed, “The effect of aging on the cutaneous microvasculature,” *Microvascular research*, vol. 100, pp. 25–31, 2015.
- [103] L. Li, S. Mac-Mary, J.-M. Sainthillier, S. Nouveau, O. De Lacharriere, and P. Humbert, “Age-related changes of the cutaneous microcirculation in vivo,” *Gerontology*, vol. 52, no. 3, pp. 142–153, 2006.
- [104] R. Ogrin, P. Darzins, and Z. Khalil, “Age-related changes in microvascular blood flow and transcutaneous oxygen tension under basal and stimulated conditions,” *The Journals of Gerontology Series A: Biological Sciences and Medical Sciences*, vol. 60, no. 2, pp. 200–206, 2005.

- [105] G. Teichert, E. Marquis, and K. Garikipati, "Machine learning materials physics: Algorithm predicts precipitate morphology in an alternative to phase field dynamics," *arXiv preprint arXiv:1806.00503*, 2018.
- [106] M. Verver, J. Van Hoof, C. Oomens, J. Wismans, and F. Baaijens, "A finite element model of the human buttocks for prediction of seat pressure distributions," *Computer methods in biomechanics and biomedical engineering*, vol. 7, no. 4, pp. 193–203, 2004.
- [107] M. Makhsous, D. Lim, R. Hendrix, J. Bankard, W. Z. Rymer, and F. Lin, "Finite element analysis for evaluation of pressure ulcer on the buttock: development and validation," *IEEE Transactions on Neural Systems and Rehabilitation Engineering*, vol. 15, no. 4, pp. 517–525, 2007.
- [108] T. Horikoshi, A. K. Balin, and D. M. Carter, "Effect of oxygen on the growth of human epidermal keratinocytes." *Journal of investigative dermatology*, vol. 86, no. 4, 1986.
- [109] F. Gottrup, "Oxygen in wound healing and infection," *World journal of surgery*, vol. 28, no. 3, pp. 312–315, 2004.
- [110] B. Lynch, C. Bonod-Bidaud, G. Ducourthial, J.-S. Affagard, S. Bancelin, S. Psilodimitrakopoulos, F. Ruggiero, J.-M. Allain, and M.-C. Schanne-Klein, "How aging impacts skin biomechanics: a multiscale study in mice," *Scientific Reports*, vol. 7, no. 1, p. 13750, 2017.
- [111] C. H. Daly and G. F. Odland, "Age-related changes in the mechanical properties of human skin," *Journal of Investigative Dermatology*, vol. 73, no. 1, pp. 84–87, 1979.
- [112] M.-S. Nguyen-Tu, A.-L. Begey, J. Decorps, J. Boizot, P. Sommer, B. Fromy, and D. Sigaudou-Roussel, "Skin microvascular response to pressure load in obese mice," *Microvascular research*, vol. 90, pp. 138–143, 2013.
- [113] S. Coleman, C. Gorecki, E. A. Nelson, S. J. Closs, T. Defloor, R. Halfens, A. Farrin, J. Brown, L. Schoonhoven, and J. Nixon, "Patient risk factors for pressure ulcer development: systematic review," *International journal of nursing studies*, vol. 50, no. 7, pp. 974–1003, 2013.
- [114] S. A. Eming, T. Krieg, and J. M. Davidson, "Inflammation in wound repair: molecular and cellular mechanisms," *Journal of Investigative Dermatology*, vol. 127, no. 3, pp. 514–525, 2007.
- [115] A. Sindrilaru, T. Peters, S. Wieschalka, C. Baican, A. Baican, H. Peter, A. Hainzl, S. Schatz, Y. Qi, A. Schlecht *et al.*, "An unrestrained proinflammatory m1 macrophage population induced by iron impairs wound healing in humans and mice," *The Journal of clinical investigation*, vol. 121, no. 3, pp. 985–997, 2011.
- [116] B. M. Delavary, W. M. van der Veer, M. van Egmond, F. B. Niessen, and R. H. Beelen, "Macrophages in skin injury and repair," *Immunobiology*, vol. 216, no. 7, pp. 753–762, 2011.
- [117] D. M. Mosser and J. P. Edwards, "Exploring the full spectrum of macrophage activation," *Nature reviews immunology*, vol. 8, no. 12, p. 958, 2008.

- [118] C. Wetzler, H. Kämpfer, B. Stallmeyer, J. Pfeilschifter, and S. Frank, “Large and sustained induction of chemokines during impaired wound healing in the genetically diabetic mouse: prolonged persistence of neutrophils and macrophages during the late phase of repair,” *Journal of Investigative Dermatology*, vol. 115, no. 2, pp. 245–253, 2000.
- [119] N. Krueger, S. Luebberding, M. Oltmer, M. Streker, and M. Kerscher, “Age-related changes in skin mechanical properties: a quantitative evaluation of 120 female subjects,” *Skin research and technology*, vol. 17, no. 2, pp. 141–148, 2011.